



RESEARCH ARTICLE

10.1029/2023JF007092

Key Points:

- Development of a depth-averaged Material Point Method for shallow landslides
- Verification of the method based on analytical solutions
- Application to snow slab avalanche release

Supporting Information:

Supporting Information may be found in the online version of this article.

Correspondence to:

J. Gaume,
jgaume@ethz.ch

Citation:

Guillet, L., Blatny, L., Trottet, B., Steffen, D., & Gaume, J. (2023). A depth-averaged material point method for shallow landslides: Applications to snow slab avalanche release. *Journal of Geophysical Research: Earth Surface*, 128, e2023JF007092. <https://doi.org/10.1029/2023JF007092>

Received 1 FEB 2023

Accepted 17 JUL 2023

Author Contributions:

Conceptualization: Johan Gaume

Formal analysis: Louis Guillet

Funding acquisition: Johan Gaume

Methodology: Johan Gaume

Project Administration: Johan Gaume

Software: Louis Guillet, Lars Blatny, Denis Steffen

Supervision: Lars Blatny, Johan Gaume

Validation: Bertil Trottet

Visualization: Louis Guillet

Writing – original draft: Louis Guillet

Writing – review & editing: Lars Blatny, Bertil Trottet, Johan Gaume

A Depth-Averaged Material Point Method for Shallow Landslides: Applications to Snow Slab Avalanche Release

Louis Guillet^{1,2}, Lars Blatny³ , Bertil Trottet³, Denis Steffen³, and Johan Gaume^{1,2,4} 

¹WSL Institute for Snow and Avalanche Research SLF, Davos, Switzerland, ²Climate Change, Extremes, and Natural Hazards in Alpine Regions Research Center CERC, Davos Dorf, Switzerland, ³School of Architecture, Civil and Environmental Engineering, EPFL, Lausanne, Switzerland, ⁴Institute for Geotechnical Engineering, ETH Zürich, Zürich, Switzerland

Abstract Shallow landslides pose a significant threat to people and infrastructure. Despite significant progress in the understanding of such phenomena, the evaluation of the size of the landslide release zone, a crucial input for risk assessment, still remains a challenge. While often modeled based on limit equilibrium analysis, finite or discrete elements, continuum particle-based approaches like the Material Point Method (MPM) have more recently been successful in modeling their full 3D elasto-plastic behavior. In this paper, we develop a depth-averaged Material Point Method (DAMP) to efficiently simulate shallow landslides over complex topography based on both material properties and terrain characteristics. DAMP is a rigorous mechanical framework which is an adaptation of MPM with classical shallow water assumptions, thus enabling large-deformation elasto-plastic modeling of landslides in a computationally efficient manner. The model is here demonstrated on the release of snow slab avalanches, a specific type of shallow landslides which release due to crack propagation within a weak layer buried below a cohesive slab. Here, the weak layer is considered as an external shear force acting at the base of an elastic-brittle slab. We verify our model against previous analytical calculations and numerical simulations of the classical snow fracture experiment known as Propagation Saw Test. Furthermore, large scale simulations are conducted to investigate cross-slope crack propagation and the complex interplay between weak layer dynamic failure and slab fracture. In addition, these simulations allow us to evaluate and discuss the shape and size of avalanche release zones over different topographies. Given the low computational cost compared to 3D MPM, we expect our work to have important operational applications in hazard assessment, in particular for the evaluation of release areas, a crucial input for geophysical mass flow models. Our approach can be easily adapted to simulate both the initiation and dynamics of various shallow landslides, debris and lava flows, glacier creep and calving.

Plain Language Summary Shallow landslides represent a significant threat to people and infrastructure. In mountainous regions, snow slab avalanches are a particular type of shallow landslide responsible for numerous casualties and important damage. Such an avalanche releases due to the failure of a weak layer buried below a cohesive slab. Despite significant progress in the understanding and modeling of such phenomena, the evaluation of the avalanche release size still remains a difficult task. This quantity is important for avalanche forecasting and is also a crucial input for hazard mapping model chains. To tackle this challenge, we develop a numerical method based on shallow water equations that simulates efficiently the release of slab avalanches over complex topography based on snow properties and terrain characteristics. The model is verified based on theoretical and numerical analysis of a state-of-the-art snow fracture experiment. Then, large scale simulations are conducted to evaluate the shape and size of avalanche release zones over different topographies. Given its low computational cost, we expect our model to have operational applications in hazard assessment, especially for the evaluation of the avalanche release size which is an important quantity for avalanche forecasting and management. The model can be easily adapted to simulate the initiation and dynamics of other processes such as debris and lava flows, glacier creep and calving.

1. Introduction

A snow avalanche consists of fast gravitational flow of a snow mass which poses a threat to snow enthusiasts and infrastructure in mountainous regions (Ancey, 2006; D. McClung & Schaerer, 2006). Among different avalanche types, dry-snow slab avalanches are responsible for most avalanche accidents and damage (Schweizer et al., 2003). Such an avalanche releases due to the failure of a weak layer buried below a cohesive snow slab (Schweizer et al., 2016). Although a lot of progress has been done regarding the understanding of slab avalanche

© 2023 The Authors.

This is an open access article under the terms of the [Creative Commons Attribution-NonCommercial License](https://creativecommons.org/licenses/by-nc/4.0/), which permits use, distribution and reproduction in any medium, provided the original work is properly cited and is not used for commercial purposes.

release processes, including the onset and dynamics of crack propagation (Bobillier et al., 2021; Gaume, Chambon, et al., 2013; Trottet et al., 2022), the evaluation of the size of avalanche release zones still remains a major issue. This difficulty impedes avalanche forecasting and hazard mapping procedures which rely on the avalanche release size as input.

Previous work tackled this obstacle through various modeling approaches. In particular, Fyffe and Zaiser (2004), Failletaz et al. (2006), and Fyffe and Zaiser (2007) developed cellular-automata to compute the statistical distribution of the release zone area. These models succeeded in reproducing power-law distributions reported based on avalanche measurements (Fyffe & Zaiser, 2004; D. M. McClung, 2003). Veitinger et al. (2016) proposed a fuzzy logic model that allows the identification of avalanche release areas on complex terrain based on topographical indicators (such as slope angle and curvature), forest indicators as well as roughness evolution induced by snow cover (progressive smoothing effect). Dynamic crack propagation in snow was simulated in 2D (depth-resolved) based on the Discrete Element Method (DEM) (Gaume, van Herwijnen, et al., 2015) and the Finite Element Method (FEM) (Gaume, Chambon, et al., 2015). Gaume and Reuter (2017) and Reuter and Schweizer (2018) later proposed novel methods to describe snow instability by combining limit equilibrium and finite element simulations. More recently Zhang and Puzrin (2022) proposed a depth-averaged finite difference method for the initiation and propagation of submarine landslides. Yet, so far, approaches combining a mechanical release model, variable material properties and complex topography are still scarce.

In these lines, advanced numerical models were recently developed. Gaume et al. (2018) proposed a Material Point Method (MPM) and constitutive snow models based on Critical State Soil Mechanics (Roscoe & Burland, 1968) to simulate in a unified manner, failure initiation, crack propagation, slab fracture, avalanche release and flow, at the slope scale. MPM is a Eulerian-Lagrangian particle-based method initially developed by Sulsky et al. (1994). Due to its ability to handle processes including large deformations, fractures and collisions, this elegant hybrid method found great interest over the last two decades, both in geomechanics, for example, for the modeling of fluid-structure interaction (York II et al., 2000), porous media micromechanics (Blatny et al., 2021, 2022), granular flows (Dunatunga & Kamrin, 2015), snow avalanche release (Gaume et al., 2019; Trottet et al., 2022), snow avalanche dynamics (Li et al., 2021), glacier calving (Wolper et al., 2021), debris flows (Vicari et al., 2022), landslides (Soga et al., 2016) and rockslides (Cicoira et al., 2022), as well as in computer graphics (Daviat & Bertails-Descoubes, 2016; Jiang et al., 2016; Schreck & Wojtan, 2020; Stomakhin et al., 2013).

After the first application of MPM to snow slab avalanches, Gaume et al. (2019) analyzed crack propagation and slab fracture patterns and reported crack speeds above 100 m/s on steep terrain. While the latter result was initially surprising, this motivated further analysis which later highlighted a transition in crack propagation regimes during the release process (Trottet et al., 2022):

- On the one hand, for short propagation distances, typically below 2 m, the failure in the weak layer occurs as a so called mixed-mode anticrack (Heierli et al., 2008), in line with field measurements (Bergfeld et al., 2022; van Herwijnen, Bair, et al., 2016) as well as recent numerical experiments using the DEM (Gaume, van Herwijnen, et al. (2015) and Bobillier et al. (2021)). The anticrack mechanism, originally introduced to explain deep earthquakes (Fletcher & Pollard, 1981) refers to a mode of compressive fracture driven by the volumetric collapse of the highly porous weak layer, which leads to the closure of crack faces and to the onset of frictional contact (Gaume et al., 2018). It was successfully introduced to explain observations of fracture propagation on flat terrain and remote avalanche triggering (Gauthier & Jamieson, 2008; Johnson et al., 2004; van Herwijnen & Jamieson, 2007) that pure shear theories (Gaume, Chambon, et al., 2013; D. McClung, 1979) failed to reproduce. In this case of short propagation distances, simulated propagation speeds in Trottet et al. (2022) are similar to those reported in classical snow fracture experiments (Propagation Saw Test (PST) (van Herwijnen, Bair, et al., 2016)) and are found to be below the Rayleigh wave speed, that is, below around 90% of the shear wave speed c_s .
- On the other hand, for propagation distances larger than the so-called supercritical crack length introduced by Trottet et al. (2022) and a slope steep enough, a pure shear mode of crack propagation is reported with speeds higher than the shear wave speed, a process called supershear fracture which was previously reported in earthquake science (Weng & Ampuero, 2020).

This transition, which occurs after a few meters suggests that the anticrack mechanism is only relevant for short propagation distances and that a pure shear model should be sufficient to estimate the release sizes of large avalanche release zones which are of interest for risk management purposes.

Motivated by this new understanding and by the high computational cost of three-dimensional simulations, we developed a depth-averaged MPM for the simulation of snow slab avalanches release with a pure shear failure model for the weak layer. This model, inspired by the one developed in Abe and Konagai (2016) for debris flows, extends the Savage-Hutter model (Savage & Hutter, 1915) in the case of elastoplasticity. After presenting governing equation and depth-integration (Section 2), we verify the model based on simulations of the so-called PST and compare numerical results to analytical solutions and 3D simulations (Section 3). Furthermore, we perform large scale simulations over generic and complex topographies and analyze the shape and size of avalanche release zones.

2. Methods

In this section, we first describe the governing conservation equations and derive their depth-integrated counterparts under the shallow water assumptions. Then, in the context of snow slab avalanches, the constitutive elasto-plastic model for the slab as well as the weak layer-slab interaction are outlined. Finally, a discretization of the equations are presented and the full depth-averaged Material Point Method (DAMPM) algorithm is summarized. A table containing all relevant symbols and notations is provided in Table D1.

2.1. Governing Equations

We denote σ the Cauchy stress tensor, \mathbf{v} the velocity field and ρ the density field of the material. Moreover, we let \mathbf{b} denote the external body force per unit mass, for example, that of gravity. The conservation of mass and momentum can then be written in conservative form as

$$\frac{\partial \rho}{\partial t}(\mathbf{x}, t) + \nabla \cdot (\rho \mathbf{v})(\mathbf{x}, t) = 0 \quad (1)$$

$$\frac{\partial(\rho \mathbf{v})}{\partial t}(\mathbf{x}, t) + \nabla \cdot (\rho \mathbf{v} \otimes \mathbf{v})(\mathbf{x}, t) = \nabla \cdot \sigma(\mathbf{x}, t) + \rho(\mathbf{x}, t)\mathbf{b}(\mathbf{x}, t), \quad \forall t > 0, \mathbf{x} \in \Omega. \quad (2)$$

where Ω is the domain where the solid is confined.

2.1.1. Depth Integration on Flat Surface

We denote h the height of the flow at any point, which can be seen as a function of the other coordinates x, y , and t . For any field $\phi : \mathbb{R}^3 \times \mathbb{R}_+ \rightarrow E$ (where E designates \mathbb{R} or \mathbb{R}^3) we introduce the associated depth-averaged field $\bar{\phi}$ such that

$$\bar{\phi} : (x, y, t) \mapsto \frac{1}{h(x, y, t)} \int_0^h \phi(x, y, z, t) dz$$

The field $\phi' = \phi - \bar{\phi}$ is defined as the difference between the field and its depth-averaged field. This implies $\int_0^h \phi' dz = 0$ and $\int_0^h \phi' \bar{\phi} dz = 0$. For each field, we also denote

$$\|\phi\|_{\infty, h}(x, y, t) := \max_{z \in [0, h]} |\phi(x, y, z, t)|. \quad (3)$$

In order to simplify the notation, we also denote $\phi|_{z=z_0}$ for any real z_0 , the function from $\mathbb{R}^2 \times \mathbb{R}_+$ to E such that

$$\phi|_{z=z_0}(x, y, t) = \phi(x, y, z_0, t)$$

2.1.1.1. Assumptions

The classic shallow-water assumptions are

- The flow depth varies gradually and is small compared to the other dimensions of the flow. This is formalized by $\varepsilon = \frac{h_0}{L} \ll 1$ where h_0 is the standard height of the flow and L the characteristic length of the release zone.
- The material is incompressible: the density ρ does not depend on position neither time.
- The flow surface is stress-free, that is, the Cauchy stress tensor on the boundary is $\sigma|_{z=h} = 0$

- Velocity fluctuations within the depths are small compared to the average velocity, in particular,

$$\frac{\|v'_x\|_{\infty,h}}{\bar{v}_x} \sim \frac{\|v'_y\|_{\infty,h}}{\bar{v}_y} = \mathcal{O}(\varepsilon). \quad (4)$$

- The vertical velocity is small compared to the other velocity components, that is,

$$\frac{\|v_z\|_{\infty,h}}{\bar{v}_x} \sim \frac{\|v_z\|_{\infty,h}}{\bar{v}_y} = \mathcal{O}(\varepsilon). \quad (5)$$

Under the assumption of incompressibility, the equation for mass conservation is therefore simplified as follows

$$\nabla \cdot \mathbf{v} = 0 \quad (6)$$

and the momentum conservation equation can thus be rewritten as

$$\frac{\partial \mathbf{v}}{\partial t} + \nabla \cdot (\mathbf{v} \otimes \mathbf{v}) = \frac{1}{\rho} \nabla \cdot \boldsymbol{\sigma} + \mathbf{b}. \quad (7)$$

2.1.1.2. Boundary Conditions

We have the following boundary conditions for the material,

$$v_z(z=h) = \frac{\partial h}{\partial t} + v_x(z=h) \frac{\partial h}{\partial x} + v_y(z=h) \frac{\partial h}{\partial y} \quad (8)$$

$$v_z(z=0) = 0. \quad (9)$$

where the first one expresses the kinematic condition on $z=h$ and the second expresses the non-porosity of the surface $z=0$.

2.1.1.3. Depth-Averaged Mass Conservation

Integration of Equation 6 for $z \in [0, h]$ yields

$$\int_0^h \nabla \cdot \mathbf{v} dz = 0,$$

which can be rewritten as

$$\int_0^h \frac{\partial v_x}{\partial x} dz + \int_0^h \frac{\partial v_y}{\partial y} dz + \int_0^h \frac{\partial v_z}{\partial z} dz = 0.$$

Applying Leibniz integration rule to each term, we obtain

$$\frac{\partial(h\bar{v}_x)}{\partial x} - v_x(z=h) \frac{\partial h}{\partial x} + \frac{\partial(h\bar{v}_y)}{\partial y} - v_y(z=h) \frac{\partial h}{\partial y} + v_z(z=h) = 0.$$

Combined with the boundary condition described in Equation 8, this leads to

$$\frac{\partial h}{\partial t} + \frac{\partial(h\bar{v}_x)}{\partial x} + \frac{\partial(h\bar{v}_y)}{\partial y} = 0, \quad (10)$$

which is the depth-averaged equation of mass conservation.

2.1.1.4. Depth-Averaged Momentum Conservation

With the same method, we integrate in the z -direction Equation 7 and get

$$\begin{aligned} \rho h \left(\frac{\partial \bar{v}_x}{\partial t} + \bar{v}_x \frac{\partial \bar{v}_x}{\partial x} + \bar{v}_y \frac{\partial \bar{v}_x}{\partial y} \right) &= \frac{\partial(h\bar{\sigma}_{xx})}{\partial x} + \frac{\partial(h\bar{\sigma}_{xy})}{\partial y} - \tau_{xz} + b_x \rho h. \\ \rho h \left(\frac{\partial \bar{v}_y}{\partial t} + \bar{v}_y \frac{\partial \bar{v}_y}{\partial y} + \bar{v}_x \frac{\partial \bar{v}_y}{\partial x} \right) &= \frac{\partial(h\bar{\sigma}_{yy})}{\partial y} + \frac{\partial(h\bar{\sigma}_{xy})}{\partial x} - \tau_{yz} + b_y \rho h. \end{aligned}$$

where $\tau_{xz} := \sigma_{xz}|_{z=0}$ and $\tau_{yz} := \sigma_{yz}|_{z=0}$. We define the depth-averaged material derivative operator for any depth-averaged field $\bar{\phi}$ as

$$\frac{d\bar{\phi}}{dt} = \frac{\partial \bar{\phi}}{\partial t} + \bar{v}_x \frac{\partial \bar{\phi}}{\partial x} + \bar{v}_y \frac{\partial \bar{\phi}}{\partial y}.$$

We can now write the non-conservative form of the momentum conservation:

$$\rho h \frac{d\bar{v}_x}{dt} = \frac{\partial(h\bar{\sigma}_{xx})}{\partial x} + \frac{\partial(h\bar{\sigma}_{xy})}{\partial y} - \tau_{xz} + b_x \rho h. \quad (11)$$

$$\rho h \frac{d\bar{v}_y}{dt} = \frac{\partial(h\bar{\sigma}_{yy})}{\partial y} + \frac{\partial(h\bar{\sigma}_{xy})}{\partial x} - \tau_{yz} + b_y \rho h. \quad (12)$$

Note that $\frac{d\bar{v}_x}{dt}$ and $\frac{d\bar{v}_y}{dt}$ are the components of the material acceleration \bar{a} . We can combine Equations 11 and 12 in the vectorial equation

$$\rho h \bar{a} = \bar{\nabla} \cdot (h\bar{\sigma}) - \tau_b + b \rho h. \quad (13)$$

where

$$\bar{a} = \begin{pmatrix} \frac{d\bar{v}_x}{dt} \\ \frac{d\bar{v}_y}{dt} \end{pmatrix}, \quad \bar{\nabla} \cdot (h\bar{\sigma}) = \begin{pmatrix} \frac{\partial(h\bar{\sigma}_{xx})}{\partial x} + \frac{\partial(h\bar{\sigma}_{xy})}{\partial y} \\ \frac{\partial(h\bar{\sigma}_{xy})}{\partial x} + \frac{\partial(h\bar{\sigma}_{yy})}{\partial y} \end{pmatrix}, \quad \text{and } \tau_b = \begin{pmatrix} \tau_{xz} \\ \tau_{yz} \end{pmatrix}.$$

Please note that the momentum conservation equation can also be projected on the z direction, which gives with the assumption 5 and the boundary condition

$$0 = -\sigma_{zz}(z=0) + \frac{\partial(h\bar{\sigma}_{xy})}{\partial x} + \frac{\partial(h\bar{\sigma}_{zy})}{\partial y} + \rho b_z h \quad (14)$$

2.1.2. Depth Integration on Complex Topography

In the previous integration, we supposed that the terrain was planar. This will be the case in most of our verification framework and applications of the model. Yet, some simulations on complex terrain will be presented which require a change of coordinate from Cartesian to curvilinear, which adds surface gradient terms to the depth-averaged momentum conservation equation. For the sake of clarity, the related mathematical framework based on the work of Bouchut and Westdickenberg (2004) and Boutounet et al. (2008) is presented in Appendix C. Note that this change of coordinate system, instead of a simple vertical projection, is necessary to recover multi-directional wave and crack propagation features.

2.1.3. Constitutive Model for Snow Slab Avalanche

The system composed of Equations 10–12 presented in the last section is not closed. To close it, we need constitutive equations relating the stress tensor σ to the deformation. In this framework, we choose an elasto-plastic model, where the slab behaves elastically until a yield stress is reached, marking the onset of permanent deformations.

2.1.3.1. Small Strain Tensor

We denote the Lagrangian coordinate X , that is, the coordinate of the undeformed material. The map of deformation φ is then defined as

$$\mathbf{u}(X, t) = \varphi(X, t) - X$$

where \mathbf{u} is the displacement of the material initially in position X between time t and time 0. The deformation gradient \mathbf{F} is defined as the gradient of the deformation map, $\mathbf{F} = \nabla \varphi(X, t)$. Note that the deformation gradient is related to the displacement by $\mathbf{F} = \nabla \mathbf{u} + \mathbf{I}$, where \mathbf{I} is the identity tensor. The Green-Lagrange strain tensor \mathbf{E} is defined as

$$\mathbf{E} = \frac{1}{2} (\mathbf{F}^T \mathbf{F} - \mathbf{I})$$

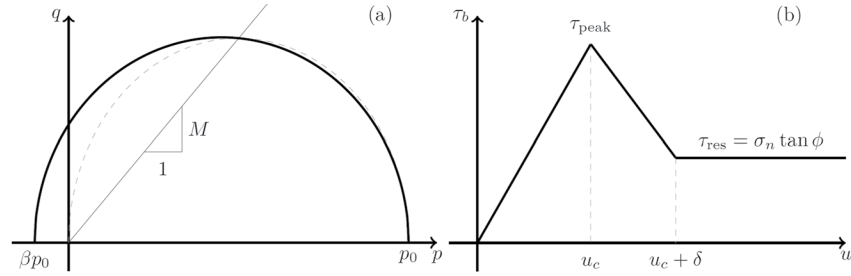


Figure 1. (a) Cohesive Cam Clay yield surface in the $p-q$ space. The dashed curve represents the cohesionless case. (b) Basal shear stress as a function of the displacement u of the slab.

which, using the expression for the deformation gradient, becomes

$$\mathbf{E} = \frac{1}{2} (\nabla \mathbf{u} + (\nabla \mathbf{u})^T + \nabla \mathbf{u} \cdot (\nabla \mathbf{u})^T).$$

We make the hypothesis that the displacement of the slab is small, we supposed then that $\|\nabla \mathbf{u}\| \ll 1$. In this condition, the Green-Lagrange strain tensor can be approximated by the small deformation strain tensor

$$\boldsymbol{\varepsilon} = \frac{1}{2} (\nabla \mathbf{u} + \nabla \mathbf{u}^T). \quad (15)$$

2.1.3.2. Elasto-Plastic Model for the Slab

We choose for the slab an additive elasto-plastic model,

$$\boldsymbol{\varepsilon} = \boldsymbol{\varepsilon}_P + \boldsymbol{\varepsilon}_E$$

with $\boldsymbol{\varepsilon}_E$ satisfying a linear elastic law,

$$\boldsymbol{\sigma} = \mathbf{D} : \boldsymbol{\varepsilon}_E \quad (16)$$

With \mathbf{D} is the fourth order elasticity tensor depending of the material elastic properties (Young's modulus and Poisson's ratio). From the last equation we have

$$\boldsymbol{\sigma} = \mathbf{D} : (\boldsymbol{\varepsilon} - \boldsymbol{\varepsilon}_P). \quad (17)$$

In order to define the onset of plastic, irreversible, deformations, a yield criterion on the stress can be introduced. Here, we choose the Cohesive Cam Clay (CCC) criterion based on Critical State Soil Mechanics (Roscoe & Burland, 1968). This model was previously proposed to model snow mechanical behavior by Meschke et al. (1996) and slab avalanche release processes by Gaume et al. (2018) and Trottet et al. (2022). This model accounts for the mixed-mode failure of snow (Reiweiger et al., 2015) and combined with a hardening/softening rule, can reproduce snow brittle fracture (Sigrist, 2006). In the space of the stress invariants p , the mean stress, and q , the von Mises equivalent stress, this criterion can be expressed as

$$q(\boldsymbol{\sigma})^2(1 + 2\beta) + M^2(p(\boldsymbol{\sigma}) + \beta p_0)(p(\boldsymbol{\sigma}) - p_0) \leq 0 \quad (18)$$

where p_0 corresponds to the consolidation pressure and directly influences the size of the yield surface; M is the slope of the cohesionless critical state line that controls the amount of friction inside the material and the shape of the yield surface; β is the cohesion parameter that quantifies the ratio between tensile and compressive strengths. This yield surface is illustrated in the space of p and q in Figure 1a. In this framework, we consider the slab as purely brittle. Therefore, if the yield criterion is not respected, we consider the slab as broken and the stress tensor is set to 0.

In the depth-averaged framework, the shear in the $x-z$ and $y-z$ plane can be neglected compared to the other stress tensor component. Under this assumption, the averaged vertical stress is

$$\sigma_{zz} = \frac{\sigma_{zz}(z=h) - \sigma_{zz}(z=0)}{2} = \frac{\rho g_z h}{2}.$$

The density ρ is assumed to be constant and h is fully determined in the MPM framework with the mass conservation (see Equation 32 in the description of the algorithm). We further assume elastic and plastic deformations only occur in the x and y direction. As h remains mostly constant in our framework, taking into account the vertical stress in the plastic deformation just correspond to a very small change of the yield criterion. Therefore the stress tensor used to compute the elastic and plastic deformation is the 2×2 matrix

$$\sigma = \begin{pmatrix} \sigma_{xx} & \sigma_{xy} \\ \sigma_{xy} & \sigma_{yy} \end{pmatrix}.$$

The stress invariant are then computed as

$$p(\sigma) = -\frac{1}{2}(\sigma_{xx} + \sigma_{yy}), \quad s(\sigma) = \sigma + p(\sigma)\mathbf{I}, \quad q(\sigma) = \sqrt{\frac{3}{2}s : s}. \quad (19)$$

Note that for uniaxial tension and uniaxial compression the value of p and q are different than if computed with the full 3×3 stress tensor. This implies the need of transforming the CCC parameters (p_0 , M , β) to have the same tensile strength, compressive strength and shear resistance in both the full 3D model and the depth-averaged model.

2.1.4. Weak Layer Modeling

The weak layer—slab interaction will be modeled by a basal force τ_b . The weak layer is considered as elastic quasi-brittle. It is rate independent and does not account for healing/sintering effects.

Such a model for the weak layer was initially introduced to simulate the growth of slip surfaces in over-consolidated clays Palmer and Rice (1973). It was then adapted to snow by D. McClung (1979) and was later used in numerous applications by for example, Gaume, Eckert, et al. (2013), Fyffe and Zaiser (2004, 2007), Zhang and Puzrin (2022), and Puzrin et al. (2019).

In Figure 1b, the basal shear force is plotted as a function of the slab displacement norm u . As long as the displacement is lower than the critical displacement, the basal stress τ_b increases with the displacement until it reaching the peak stress τ_{peak} . Then, in order to model the quasi-brittle failure of the weak layer, the stress decreases down to the residual stress $\tau_{\text{res}} = \sigma_n \tan \phi$ with σ_n the normal stress at the base of the material and ϕ the basal frictional angle between the slab and the weak layer. This represents the Coulomb model for the dry friction when the sliding of the slab on the weak layer occurs. The softening phase is associated with a plastic displacement δ .

In the domain $u < u_c$ the model acts as a spring between the slab and the weak layer whose stiffness k_{WL} is the slope of the linear part. k_{WL} can be related to the geometrical and mechanical characteristics of the weak layer as

$$k_{\text{WL}} = \frac{G_{\text{WL}}}{D_{\text{WL}}},$$

where G_{WL} is the shear modulus and D_{WL} is its thickness. We can thus give the expression of τ_b as a function of u :

$$\tau_b(u) = \begin{cases} k_{\text{WL}} u, & \text{if } u < u_c \\ \tau_{\text{res}}, & \text{if } u > u_c + \delta \end{cases} \quad (20)$$

We can also define the cohesion C_{WL} between the slab layer as

$$C_{\text{WL}} = \tau_{\text{peak}} - \tau_{\text{res}} = \tau_{\text{peak}} - \sigma_n \tan \phi.$$

As $u_c = \tau_{\text{peak}}/k_{\text{WL}}$, the weak layer model requires three parameters; the peak stress τ_{peak} , thickness D_{WL} and shear modulus G_{WL} .

2.2. Numerical Model: DAMPM

2.2.1. Discretization

In this section we summarize the depth-averaged version of the MPM algorithm used to solve Equations 11 and 12. A sketch of the scheme is illustrated in Figure 2. A depth-averaged version of MPM has been introduced

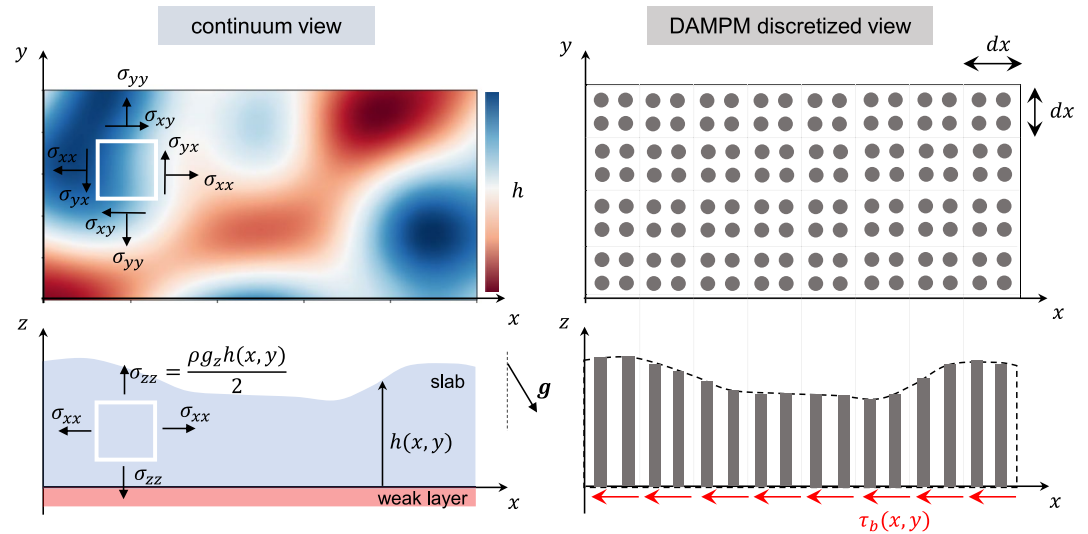


Figure 2. Illustration of some model assumptions and DAMPM discretization.

by Abe and Konagai (2016) to simulate shallow debris flows. The principle of the method is very close to the classical MPM. We discretize the material domain with Lagrangian points, which unlike in classical MPM, are now “columns” with a certain variable height. In addition to their height, these columns store information of velocity, stress and plastic deformation. Furthermore, a background Eulerian grid is used to facilitate uncomplicated spatial differentiation. An interpolation scheme is used to transfer quantities between columns and grid nodes.

As shown in detail in Appendix A, the weak form discretization of Equation 13 in direction x is given by

$$m_i^k a_{x,i}^k = (f_{x,i}^{\text{ext},k} + f_{x,i}^{\text{int},k}) \quad \forall i \in \{1, \dots, n_g\}. \quad (21)$$

where the forces at each node are computed via an interpolation over the particles as follows:

$$f_{x,i}^{\text{ext},k} = \sum_{p=1}^{n_p} \rho V_p b_{x,p} N_{ip}^k \quad (22)$$

$$f_{x,i}^{\text{int},k} = - \sum_{p=1}^{n_p} \left[V_p \bar{\sigma}_{xx,p}^k \frac{\partial N_{ip}^k}{\partial x} + V_p \bar{\sigma}_{xy,p}^k \frac{\partial N_{ip}^k}{\partial y} + \tau_{xz,p}^k N_{ip}^k \right]. \quad (23)$$

In these equations,

- V_p is the constant volume of material element p
- N_{ip}^k is the evaluation of the interpolation function centered at the grid node i and evaluated at the center of the material element p at time t^k
- $\bar{\sigma}_{xx,p}^k$ is the depth-averaged stress of the material element p in the $x - x$ direction at time t^k
- $\tau_{xz,p}^k$ is the basal force in the x direction of the material element p at time t^k
- $b_{x,p}$ is the projection of the volumetric forces in the x direction of the material element p
- n_p and n_g are respectively the number of material particles and grid nodes.

The coefficient m_i^k are the coefficient of the lumped mass matrix defined on the grid as

$$m_i^k = \sum_{j=1}^{n_g} m_{ij}^k = \sum_{p=1}^{n_p} m_p N_{ip}^k.$$

2.2.2. Algorithm

Here, the algorithm for one time step of the Depth-Averaged Material Point Method is outlined. It relies on the elastic predictor—plastic corrector scheme of computational elastoplasticity, where a trial stress state is computed

and projected back to the yield surface if permanent deformations occurred (de Souza Neto et al., 2008). A summary of the DAMPM algorithm is provided in Algorithm 1 (Appendix B).

1. An Eulerian background grid with cell size Δx is created to cover the material domain. If $t > 0$, the grid is only extended or reduced to cover the updated material domain.
2. The mass and velocity on the grid nodes at time t^k is interpolated from the particles in what is called the Particles to Grid (P2G) step,

$$m_i^k = \sum_{p=1}^{n_p} m_p N_{ip}^k$$

$$\bar{\mathbf{v}}_i^k = \sum_{p=1}^{n_p} \bar{\mathbf{v}}_p^k m_p N_{ip}^k / m_i^k \quad (24)$$

Note the interpolation of the momentum divided by the lumped mass matrix component, guaranteeing conservation of momentum between material points and grid nodes. The interpolation functions used in this study are cubic B-splines,

$$N(u) = \begin{cases} \frac{1}{2}|u|^3 - |u|^2 + \frac{2}{3} & \text{if } |u| \leq 1 \\ \frac{1}{6}(2 - |u|)^3 & \text{if } |u| \in [1, 2] \\ 0 & \text{if } |u| \geq 2 \end{cases} \quad (25)$$

such that

$$N_{ip} = N_i(\mathbf{x}_p) = N\left(\frac{x_i - x_p}{\Delta x}\right)N\left(\frac{y_i - y_p}{\Delta y}\right).$$

3. Based on the stress tensor $\bar{\boldsymbol{\sigma}}_p^k$ and the external force \mathbf{b}_p^k on the particles, the forces $\mathbf{f}_i^{\text{int},k}$ and $\mathbf{f}_i^{\text{ext},k}$ on the grid nodes are computed as described in Equations 22 and 23.
4. Using Equation 21, the acceleration on the grid nodes is obtained from the previously computed forces

$$\bar{\mathbf{a}}_i^k = (\mathbf{f}_i^{\text{int},k} + \mathbf{f}_i^{\text{ext},k}) / m_i^k \quad (26)$$

from which a grid velocity can be computed

$$\bar{\mathbf{v}}_i^L = \bar{\mathbf{v}}_i^k + \Delta t \bar{\mathbf{a}}_i^k \quad (27)$$

5. Instead of immediately computing the increment of strain and stress we interpolate the velocity and the position on the particles, in what is called the Grid to Particles (G2P) step,

$$\bar{\mathbf{v}}_p^{k+1} = \bar{\mathbf{v}}_p^k + \sum_{i=1}^{n_g} \left((\Delta t \bar{\mathbf{a}}_i^k) C_{\text{flip}} + \bar{\mathbf{v}}_i^L (1 - C_{\text{flip}}) \right) N_{ip}^k \quad (28)$$

$$\mathbf{x}_p^{k+1} = \mathbf{x}_p^k + \Delta t \sum_{i=1}^{n_g} \bar{\mathbf{v}}_i^L N_{ip}^k \quad (29)$$

where C_{flip} is the FLIP (Fluid Implicit Particle in Cell)-PIC (Particle In Cell) ratio (Stomakhin et al., 2013). $C_{\text{flip}} = 0$ corresponds to a pure PIC (Particle In Cell) scheme where we obtain particle velocity as an interpolation from grid velocity directly. On the other hand, $C_{\text{flip}} = 1$ corresponds to a pure FLIP (FLuid Implicit Particle in cell) scheme where only the increment of grid velocity is interpolated, thus reducing dissipation at the cost of stability. In this work, we use $C_{\text{flip}} = 0.9$ as a balance between reducing dissipation and maintaining stability.

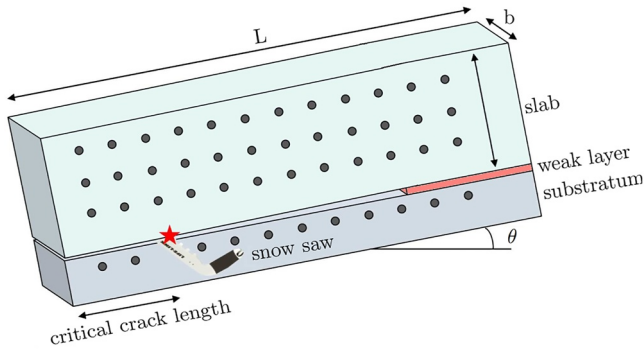


Figure 3. Schematic of the Propagation Saw Test.

6. Following the so-called MUSL (Modified Update Stress Last) algorithm (Sulsky et al., 1995), the grid velocities are interpolated from the updated particle momentum before they are used to calculate the strain increment.

$$\bar{\mathbf{v}}_i^{k+1} = \frac{1}{m_i^k} \sum_{p=1}^{n_p} m_p \bar{\mathbf{v}}_p^{k+1} N_{ip}^k \quad (30)$$

While this step is optional, it improves stability.

7. Relying on the grid velocities, Equation 15 gives a trial strain increment on the particles,

$$\Delta \epsilon_p^{\text{trial}} = \frac{\Delta t}{2} \left(\sum_{i=1}^{n_g} \nabla N_{ip}^k (\bar{\mathbf{v}}_i^{k+1})^T + \sum_{i=1}^{n_g} (\nabla N_{ip}^k)^T \bar{\mathbf{v}}_i^{k+1} \right) \quad (31)$$

8. The height of each particle is updated according to the strain increment,

$$h_p^{k+1} = \frac{h_p^k}{1 + \text{tr}(\Delta \epsilon_p^{\text{trial}})} \quad (32)$$

9. The trial stress tensors can be computed depending on

$$\bar{\boldsymbol{\sigma}}_p^{\text{trial}} = \mathcal{D}^e : \epsilon_p^{\text{trial}} \quad (33)$$

with \mathcal{D}^e the fourth order tensor in plane stress model.

10. If the trial stress tensor satisfies the yield criterion, the trial strain and stress tensors are taken as the new strain and stress tensors, respectively, that is,

$$\epsilon_p^{k+1} = \epsilon_p^{\text{trial}} \quad (34)$$

$$\bar{\boldsymbol{\sigma}}_p^{k+1} = \bar{\boldsymbol{\sigma}}_p^{\text{trial}} \quad (35)$$

Otherwise, the stress vanishes as we assume the material to be purely brittle

$$\bar{\boldsymbol{\sigma}}_p^{k+1} = \mathbf{0}$$

11. An adaptive time-stepping is used where the time step Δt according to two conditions. The first is the Courant-Friedrich-Lewy (CFL) condition, resulting in

$$\Delta t \leq \frac{C_{\text{cfl}} \Delta x}{\max_{p=1, \dots, N_p} \|v_p\|_{L^2}} \quad (36)$$

where $C_{\text{cfl}} < 1$. In addition, the time step Δt must be smaller than the time an elastic wave takes to travel a distance Δx , thus we impose

$$\Delta t \leq C_{\text{elastic}} \frac{\Delta x}{\sqrt{E/\rho}} \quad (37)$$

where $C_{\text{elastic}} < 1$.

3. Results

In order to validate our model we perform simulations of the so-called PST. The PST is a classical snow fracture experiment used by avalanche researchers and practitioners to evaluate crack propagation propensity. It consists of isolating a column of snow and cutting through a previously identified weak layer, using a snow saw. This cutting procedure amounts to create a crack of increasing length until a so-called critical crack length is reached leading to self-sustained crack propagation. The PST setup is sketched in Figure 3.

First, simulations with an elastic slab are made, where we can compare to analytical solutions for the critical crack length, the onset of crack propagation and the slab tensile failure distance. Second, simulations with a

Table 1
Table of Parameters for the Different Simulations Presented in This Work

		Case 1	Case 2	Case 3	Case 4
Geometry	Length L_1 (m)	40	40	50	40
	Width L_2 (m)	0.3	0.3	50	120
	Slope angle θ ($^\circ$)		45		
Slab	Density ρ ($\text{kg}\cdot\text{m}^{-3}$)		250		
	Height h (m)		0.5		
	Young's modulus E (MPa)		10		
	Poisson's ratio ν		0.3		
	Friction angle ϕ ($^\circ$)		27		
	Pre-consolidation pressure p_0 (kPa)	—	30	—	15
	Slope of critical state line M	—	1.7	—	1.7
Weak layer	Cohesion parameter β	—	0.1	—	0.1
	Thickness D_{WL} (m)		0.125		
	Young's modulus E_{WL} (MPa)		1		
	Poisson's ratio ν_{WL}		0.3		
	Shear strength τ_{peak} (Pa)		1,450		
Numerical	Cell size Δx (cm)	2	2	10	10
	CFL constraint C_{cfl}		0.5		
	Elastic wave constraint C_{elastic}		0.5		
	FLIP/PIC ratio C_{flip}		0.9		

Note. The values in the middle of the table are valid for all the cases.

elastic-brittle slab are performed in which we evaluate the distance to the first slab fracture and compare to analytical relations. Third, we perform multi-directional fracture simulations to study crack propagation speeds in down/up slope and cross slope directions in a three dimensional slope configuration. Finally, we analyze slab fracture characteristics in mixed-mode crack propagation simulations.

Table 1 shows parameters used throughout all simulations. Note that the mechanical properties of the slab and the weak layer are taken based on literature data. A typically measured slab density of 250 kg m^{-3} was taken (van Herwijnen, Gaume, et al., 2016). The Poisson's ratio, elastic modulus of the slab and weak layer (ν , ν_{WL} , E , E_{WL}) are taken based on data collected by Mellor (1975). Similarly, the slab plasticity parameters p_0 , β , and M are evaluated based on compressive, shear and tensile strengths values from Mellor (1975). The friction angle of the weak layer is taken from experimental data from Van Herwijnen and Heierli (2009). The weak layer shear strength was chosen within the range reported by Jamieson and Johnston (2001) based on shear frame measurements.

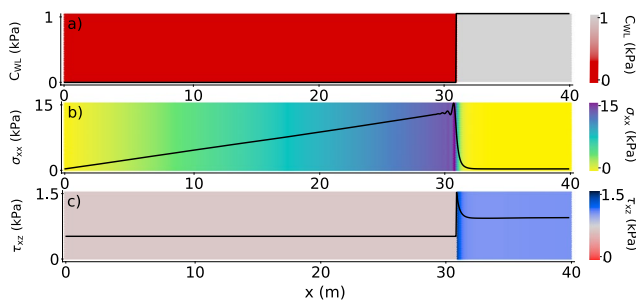


Figure 4. Top view of a Propagation Saw Test simulation. From top to bottom, we represented the cohesion, the longitudinal stress and the basal stress (see Movie S1).

3.1. PST Crack Propagation With an Elastic Slab

Figure 4 show the cohesion (a), the tensile stress (b) and the shear stress in the weak layer (c) in a PST simulation during dynamic crack propagation at time ($t^* = t - t_c = 0.25 \text{ s}$, t_c := time corresponding the onset of crack propagation). The parameters for this simulation correspond to case 1 of Table 1. The crack tip is identified based on cohesion which shows a transition between the initial value of $\approx 1 \text{ kPa}$, and zero (Figure 4a). This transition is very sharp because the plastic softening displacement δ was set to zero. This transition in cohesion is directly linked to the shear stress in the weak layer τ_{xz} which reaches the weak layer strength $\tau_p = 1.45 \text{ kPa}$ (Figure 4b). The shear stress is characterized by three zones: far from the crack tip in the undisturbed region, the shear stress is equal to the stress induced by the projected slab weight $\tau_g = \rho gh \sin \theta$. Behind the crack tip, cohesion is zero and thus the shear stress is equal to the residual

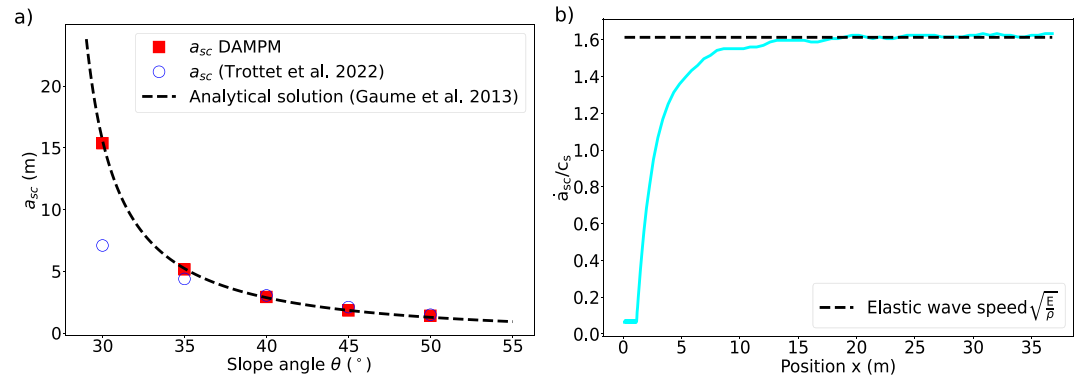


Figure 5. a) comparison between the simulated super critical length using DAMPM, a 3D model (Trottet et al., 2022) and the analytical solution in quasi-static regime for different angle. b) Crack velocity profile as a function of the position.

frictional stress. In between these two regions, the shear stress decreases exponentially from its maximum value τ_p to τ_g with a characteristic length Λ (see below). In addition, the tensile stress in the slab increases linearly from the origin to the crack tip, where it is maximum. It then decreases exponentially to zero ahead of the crack. We note some small oscillation behind the crack tip which are very likely due to the limited amount of damping in our simulations.

In a spirit of verification, we performed several simulations with different values of the slope angle and computed the (super) critical crack length corresponding to the onset of crack propagation. We recall that due to the depth-averaged nature of the model, we do not simulate the anticrack propagation regime but only the supershear mode of crack propagation as described in Trottet et al. (2022). We thus refer to critical lengths as super critical in the later. In our particular case (PST) and with the assumption presented above, an analytical solution can be found (Gaume, Chambon, et al., 2013) and is given below:

$$a_{sc} = \Lambda \left(1 - \frac{\tau_p}{\tau_g} \right) \frac{\tan(\theta)}{\tan(\theta) - \tan(\phi)} \quad (38)$$

Figure 5a shows the supercritical crack length a_{sc} as a function of slope angle for 3D simulations (Trottet et al., 2022), depth-averaged simulations (this study) and the analytical solution in Equation 38. We report an excellent agreement between our model and the expected solution. In fact the agreement is better than for 3D simulations, which was expected. Indeed, in 3D simulation, the collapse amplitude leads to a reduction in the effective friction coefficient of the weak layer and thus a reduction of a_{sc} close to the frictional limit.

Another verification can be made by analyzing the crack propagation speed \dot{a}_{sc} limit (Figure 5b). We observe a strong increase in propagation speed between a_{sc} and a distance of around 10 m where the speed levels off at an asymptotic value close to $1.6 c_s = \sqrt{E/\rho}$. This is in line with the results of Trottet et al. (2022) and with expectations regarding the form of the 1-D equations which suggest that we should converge to the longitudinal wave speed.

3.2. PST Crack Propagation With an Elastic-Brittle Slab

In this section, we relax the assumption of a purely elastic slab and perform the simulation with a slab failure criterion (see Section 2.1.3). Figure 6 shows the cohesion (a), the basal stress (b) the height (c), the longitudinal stress (d) and finally the velocity (e) as a function of the position x of such a simulation at time $t^* = 0.3$ s. The parameters used for the simulation are the same as the elastic simulation (see case 2 of Table 1) and with a tensile strength $\sigma_t = 7$ kPa.

Tensile failures are characterized by a decreasing peak in the height profile (Figure 6c). In this simulation, we observe 3 different failures at position $x \sim 10$ m, $x \sim 20$ m, and $x \sim 30$ m. As the fracture gap is growing with time, the height decrease is more pronounced in the first fracture. At each fracture interface, the slab stress is set to zero. As there is almost no damping in our simulations, we have small spatial oscillations in the tensile stress profile. In addition and for the same reason, the tensile stress is oscillating in time between compression and tension between two fractures, oscillations which do not attenuate in time (this can only be seen by watching the temporal evolution of these profiles in Movie S2). At each failure, we observe a discontinuity of the down-slope velocity. The value of the velocity between two fractures is oscillating in time around a plateau in relation to

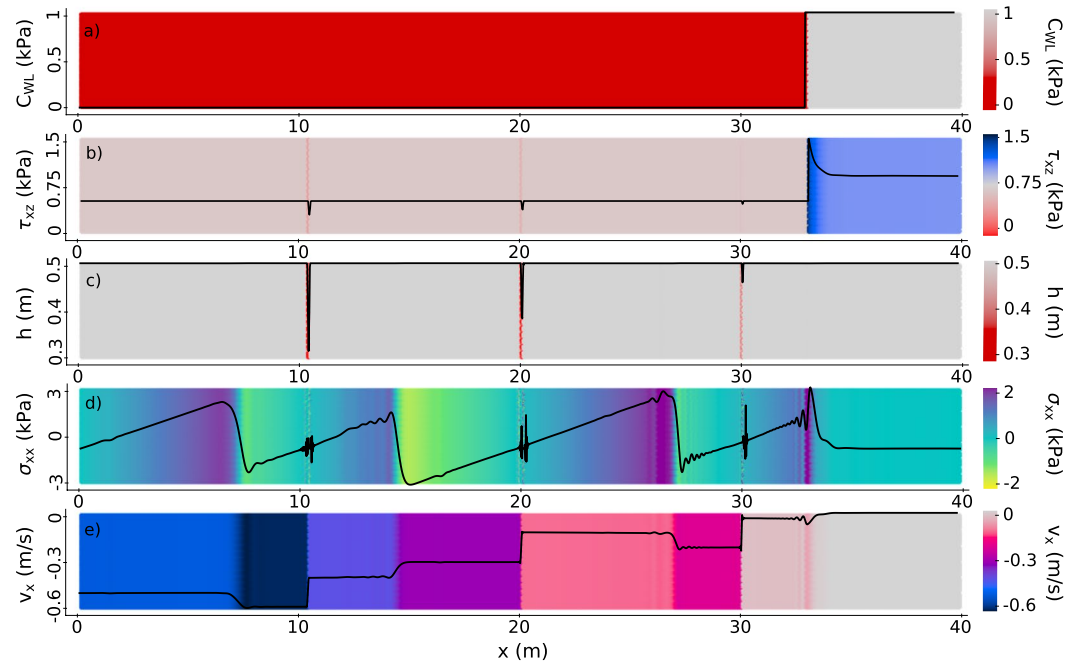


Figure 6. Top view of a Propagation Saw Test simulation in which tensile fracture of the slab is enabled. From top to bottom, we represented the cohesion, the basal stress, the height, the longitudinal stress and the tangential velocity (see Movie S2).

the longitudinal stress oscillation described above. As the residual friction is computed as $\tau_r = \rho g h \tan(\phi)$, the decreasing peak in the height profile at each fracture will also be observed in the basal forces (Figure 6b). The tensile fractures in the slab do not stop the propagation of the crack in the weak layer. The fractures have also very little impact on the profile of the stress and the basal force after the crack tip, which are the same as in the simulations with a purely elastic slab. Again, the discontinuity of the basal force profile at the crack tip is due to δ , the softening length of the weak layer which is equal to zero in the presented simulations.

In the 1D quasi-static pure shear model, we have an explicit expression of the longitudinal stress in the slab (Gaume, Chambon, et al., 2013) and therefore have an analytical expression of what must be the tensile fracture length l_t . We can now verify the model by comparing the simulated l_t and the analytical one in Figure 7a. There are 2 cases in the simulations: either the first tensile fracture occurs during the sawing phase (quasi static regime with $l_t \leq a_{sc}$), or it occurs after the sawing phase (dynamic case with $l_t \geq a_{sc}$). The simulated tensile fracture length in the quasi-static case is very close to the theoretical one, which give us a strong verification for the stress computation within the slab. However, we remark that the simulated tensile fracture length in the dynamic case is lower than the theoretical one. This phenomena occurs on the one hand because we neglected the dynamic term in the expression of the theoretical l_t and on the other hand this can be related to the oscillations in the longitudinal stress (see Figure 4).

In addition, if we analyze the velocity profile of the crack tip as a function of the position, we observe mainly two cases depending of the value of σ_r . Either we have a crack arrest: the propagation of the crack in the WL is stopped when the tensile fracture occurs (magenta curve in Figure 7b). If the tensile strength is large enough, the crack continues after the slab fracture. The later slows down the crack velocity, which increases again toward the longitudinal wave speed.

3.3. 2D Crack Propagation With an Elastic Slab

Previous simulations were performed with one main crack propagation direction (1D). In this section, we perform two dimensional simulations of crack propagation in the weak layer for a purely elastic slab. The output of such simulation at time $t^* = 0.2$ s are given in Figure 8. The represented quantities are the cohesion (a), the shear stress within the slab (b), the longitudinal stress (down/up slope) (c), the velocity in the slope direction (d), the basal forces (e) and the transversal stress (cross-slope) (f). The parameters used for the simulation are given in case 3 of Table 1. After the initial loading phase, we manually and progressively remove a cohesion circle at the center of

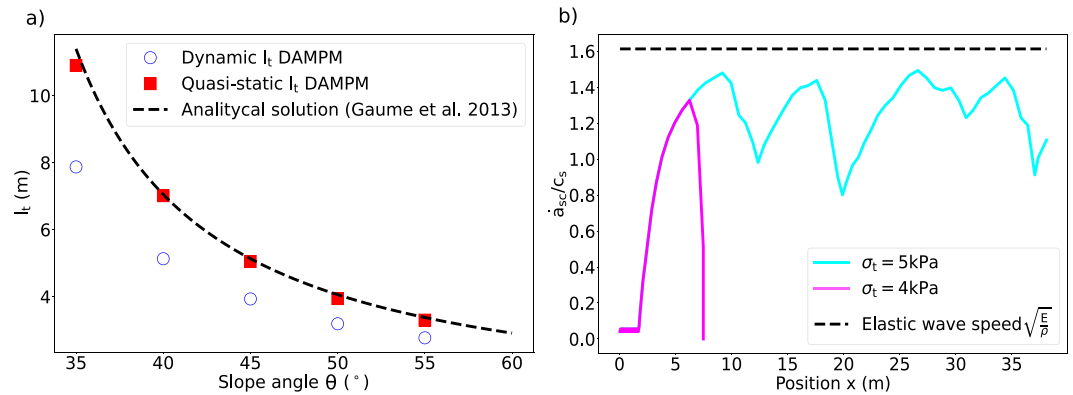


Figure 7. a) comparison between the simulated tensile length in quasi static and dynamic regimes and the analytical tensile length (quasi static). b) crack velocity profile as a function of the position for two different tensile failure criteria.

the slab until observing self propagation of the crack in both direction. The crack in the weak layer grows with a shape resembling that of an ellipse. The shape of the crack area appears to converge toward a self similar shape as both cross slope and down-slope and cross-slope crack velocity converges (see also Movie S3). From Figure 8e, we observe that, as in the PST simulation, the basal force is equal to the frictional stress τ_r where the cohesion is set to zero. It reaches then τ_p at the edge of the crack area before converging toward τ_g . We also observe that the crack propagation is mostly driven by the shear within the slab σ_{xy} in the cross slope direction and by the longitudinal stress in σ_{xx} in the up-slope/down-slope direction. The transversal stress σ_{yy} is indeed far less in norm than the other component of the plane stress tensor.

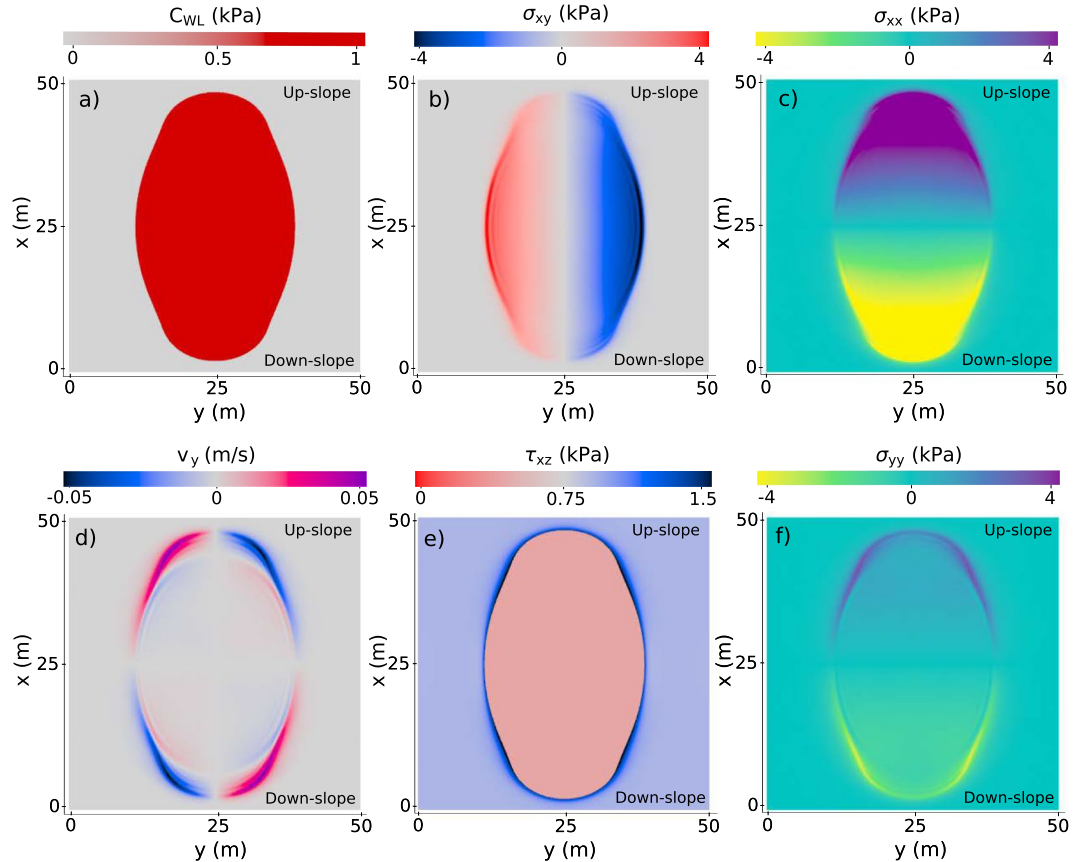


Figure 8. Top view of a different outputs of 2D crack propagation with a purely elastic slab (see Movie S3).

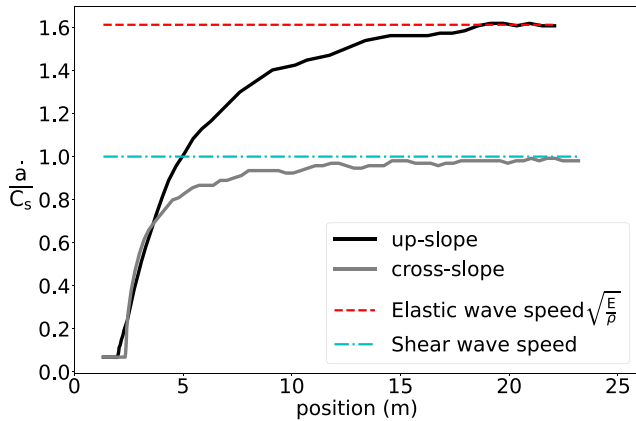


Figure 9. Cross-slope and up-slope crack velocities.

If we focus on the crack velocity profile in the x and y direction (Figure 9), we see that the up-slope crack velocity converges to the longitudinal wave speed c_p but the cross-slope crack velocity converges toward c_s . This comforts the fact that the up slope crack propagation is driven by the longitudinal wave and the cross-slope propagation is driven by the shear wave.

3.4. 2D Crack Propagation With an Elastic-Brittle Slab

In this section, we no longer assume the slab to be purely elastic and perform simulations in which the slab can break according to the CCC model presented in the Methods. This will allow us to evaluate the shape of the avalanche release area. Figure 10 shows four physical outputs of such a simulation during the formation of the release area. The parameters used for this simulation can be found in case 4 of Table 1. We have from left to right the velocity in the slab v_x (a), the weak layer shear stress τ_0 (b), the height (c) and the cohesion (d). The CCC parameters used in this simulation ($\beta = 0.1$, $p_0 = 15$ kPa, $M = 1.7$) allowed us to model realistic tensile, shear

and compressive strengths (see Section 2). In the height output (Figure 10a), the red color corresponds to tensile failures with a decrease of the height. On the other hand, blue and dark blue colors correspond to compressive failures with an increase in height. We observe that the area below the crown (tensile failure) corresponds to the failed part of the weak layer in which cohesion is zero. In this area, the shear stress in the weak layer is equal to the residual frictional stress and we remark small stress variations induced by local height variations induced by the slab fracture. Above the crown, the stress in the weak layer is almost equal to the shear stress induced by the slab weight τ_g with small oscillations related to elastic wave propagation (simulation with almost no damping). Similar to the observations made above in the elastic slab case, we have strong shear stress concentrations reaching τ_p at the weak layer crack tip. Ultimately, the broken slab pieces start to slide with different velocities and a negative velocity gradient from the center of the simulation to its edge. It was checked that the system dimensions and wave reflections at the boundaries (observed in Movie S4) did not affect the general shape of the release zone.

4. Discussion

In this paper, we proposed a depth-averaged Material Point Method (DAMPM) to simulate crack propagation and slab fracture during the release process of dry-snow slab avalanches. This study was motivated by recent

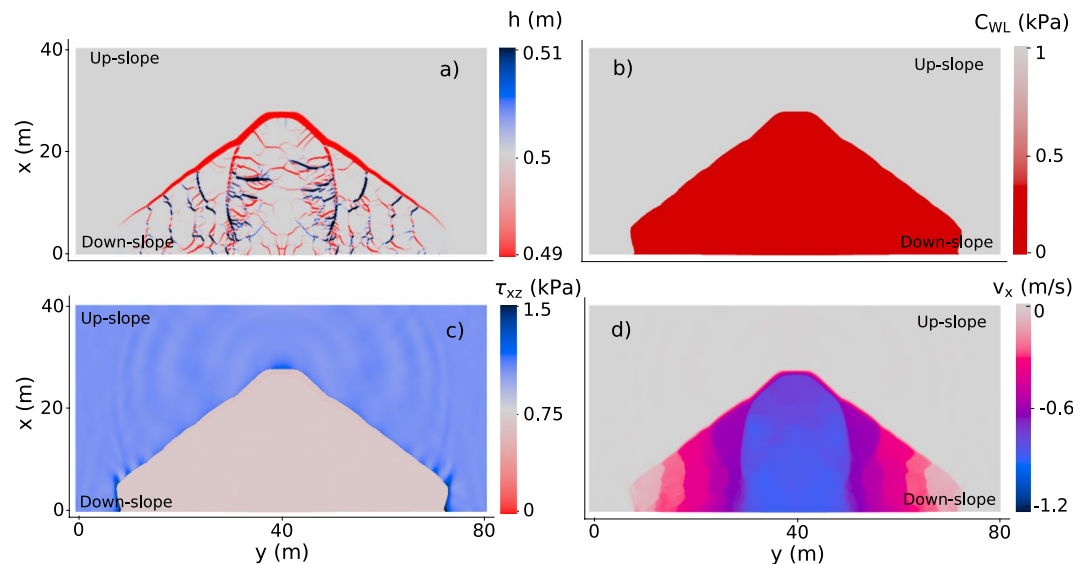


Figure 10. Top view of 3D DAMPM simulation with a plastic model for the slab (see Movie S4).

findings by Trottet et al. (2022) evidencing a transition from anticrack to supershear fracture after a few meters of propagation in the weak layer. In this supershear regime, slab tension drives the fracture whereas slab bending can be neglected leading to pure shear (mode II) crack propagation in the weak layer. These supershear avalanches propagate with intersonic crack velocities and are believed to generate large avalanche release zones. Hence, for the sake of risk management, in which 100 or 300 years return period avalanches are usually considered, the assumption of weak layer shear failure appears appropriate. Yet, it is important to recall that by construction, the present model is unable to simulate crack propagation on low angle terrain and remote avalanche triggering. The DAMPM model presented in this article is more efficient in terms of computational time compared to the 3D MPM of Trottet et al. (2022). For instance, the DAMPM PST simulation in case 1 and 2 have around 150,000 particles each and would require more than 1 million particles in 3D. Similarly, the DAMPM simulation shown in case 3 has around 1 million particles and would require 10 times more in 3D. Our approach is thus naturally faster than 3D DEM or FEM models. Compared to limit equilibrium analysis, our approach has the main advantage to be able to capture the dynamic interplay between weak layer failure and slab fracture, thus enabling the evaluation of release zones.

After verification of the method based on analytic solutions, it was applied to three dimensional terrain with or without enabling slab fractures. It was found that the DAMPM model was able to reproduce the quasi-static prediction of the super critical crack length with a classical shear band propagation approach. In addition, the onset of slab fracture was well reproduced in quasi-static conditions. Finally, it was verified that the crack propagation speed in the up/down slope direction was reaching the longitudinal wave speed c_p . On the other hand, the cross slope crack speed converges to c_s . This leads to an elliptical propagation shape. With their depth-averaged finite difference model, (Zhang & Puzrin, 2022) reported different types of shapes. By restricting the motion in the lateral direction, they also report an elliptical shape. However, without this restriction, they report a “peanut” propagation shape. This particular shape is due to the non-symmetry of the lateral slab velocity. Surprisingly, while this non-symmetry is also present in our simulations, a “peanut” shape was initially not observed. It is only when the scale of the simulation was increased or if the characteristic length Λ was decreased (e.g., through a decrease of the slab elastic modulus) that this peculiar shape was recovered. As a consequence, the shape of the ellipse is not self-similar in time. This is induced by the mismatch of the longitudinal and lateral crack propagation speeds.

It is important to note that, in principle, based on theoretical considerations (Broberg, 1989b), the Rayleigh wave speed c_R should not be exceeded in Mode II. In our study, slab bending and shear within the depth are not taken into account due to the plane stress assumption made for depth-averaging. Hence, in our model, there is no reason why the propagation speed should be limited by c_R . This is why in our case, we have a smooth increase of the speed toward the longitudinal wave speed c_p . In 3D simulations, a daughter supershear crack nucleates ahead of the main fracture with a speed which continuously increases toward c_p , while crossing the forbidden region between c_R and c_s (Bergfeld et al., 2022; Bizzarri & Das, 2012; Gaume et al., 2019). We obviously cannot reproduce the discontinuity reported in 3D simulations, but the temporal evolution of the supershear crack speed is in line with the latter 3D simulation. Furthermore, in mode III (cross-slope), we obtain a convergence to c_s in line with previous theoretical work (Broberg, 1989a).

Allowing for slab mixed-mode fracture in DAMPM allowed us to obtain interesting “hand fan” shape for the release area. In details, the half angle at the top of the fan is around 50° for the simulation in Figure 10. While we cannot claim validation, this shape is clearly in line with field observations of artificially triggered avalanches as seen in Figure 11 in which the half fan angle appears to be between 40 and 50° . In our model, the detailed shape is influenced by the choice of plastic parameters, but the overall shape remains similar. We also performed a larger simulation on a wider slope including a convex top ridge and concave transition to flat terrain (Figure 12). Interestingly, this simulation shows a race between crack propagation in the weak layer and slab fractures, leading to lateral en-echelon failures, a process often reported in the field (Bergfeld et al., 2022). The overall shape differs from the pictures in Figure 11, but is in line with observation of larger avalanches in which the crown fracture is very often irregular and impacted by topography. In this simulation, it is interesting to report that the tensile crown failure occurs for a slope angle around 35° and that the stauwall failure is occurring for an angle very close to the friction angle of the weak layer. To obtain mixed-mode slab fractures, the model assumed a complete loss of strength once the yield criterion is met. While this assumption can be well justified for tension, it can raise questions for compression. The reason behind this simplification



Figure 11. Avalanche release photographs. Credit from left to right: Rémi Petit, Dominique Daher and Isabelle Sabater.

is related to the nature of our model. In real life, the stauwall is under compression but after yielding, a shear band forms and the slab moves above the resting snowpack without any compressive resistance. As this process cannot obviously not be simulated in such a depth-averaged framework, we decided to make the simplest assumption. In addition, as we are interested only in the release phase, the simulation is stopped once the compressive stauwall is formed.

The DAMPM model presented here was inspired by the work of Abe and Konagai (2016) proposed to model the dynamics of debris flows. Our model, however, was developed to simulate a different process, namely the release of shallow landslides. It contains numerous improvements compared to the latter study. In particular, the linear shape functions used in Abe and Konagai (2016) are known to produce cell-crossing errors and spurious stress oscillations. This is addressed in our approach by using a higher order MPM with cubic B-splines. Another important improvement is the consideration of curvilinear coordinates that prevents

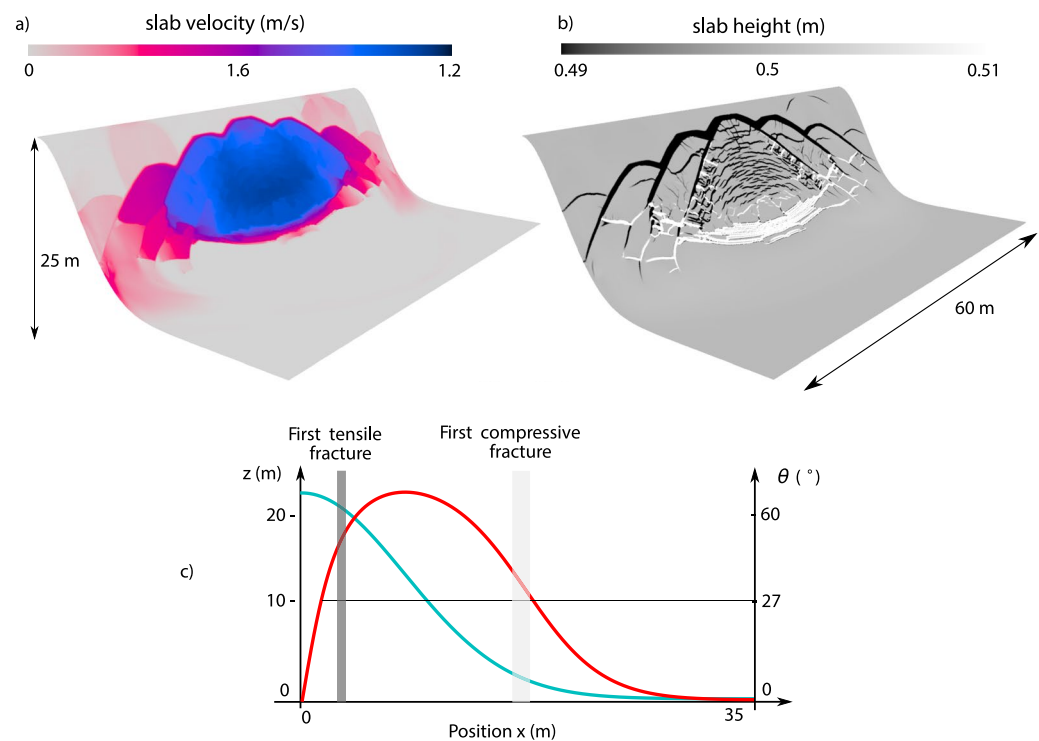


Figure 12. Simulation outputs with variation of the topography. a) Tangential velocity distribution in the slab. b) Height distribution in the slab. c) Altitude profile (blue) and slope angle profile (red) at the middle of the width with the first tensile/compressive failure marked (see Movie S5).

projection errors on simulations with complex topography. In addition, our model has strong similarities with the cellular automata model developed by Fyffe and Zaiser (2004, 2007). In their study, they were able to simulate both weak layer shear failure and slab fracture, based on finite differences. The weak layer model is almost identical but their slab constitutive law does not consider mixed-mode failure. The more rigorous numerical scheme together with a more complete description of the slab mechanical behavior in our model very likely contributed to the different release shapes in our respective studies. In particular, they report a release zone which is larger in the downslope direction than in the cross slope direction. This contrasts with our results and with field observation of avalanche release zones made by D. M. McClung (2009). The latter author reports a ratio between cross-slope and down/up slope dimensions of the release area to be around 2.1 for unconfined conditions. The shape of our release area also differs from that of Zhang and Puzrin (2022) with a mismatch very likely due to a different slab constitutive model (von Mises vs. CCC). Regarding the weak layer mechanical behavior, we assumed a rate-independent model without sintering/healing effects. Interestingly, Fyffe and Zaiser (2004) showed that sintering/healing of damaged regions almost did not affect the overall stability of their simulated slopes. For our application (artificial avalanche release) involving large strain rates, neglecting healing seems to be a reasonable assumption (Reiweger, 2011). However, a rate-dependent model should be implemented in the future to study the release of natural slab and glide snow avalanches.

Concerning numerical limitations, our DAMPM implementation is based on a FLIP/PIC transfer scheme where particles quantities are transferred to grid nodes using cubic splines with a support of $2\Delta x$. With this particular scheme, a balance must be found between accuracy (pure FLIP) and stability (pure PIC). Here we chose to promote accuracy with a FLIP/PIC ratio of 0.9 and thus limited damping. The numerical oscillations increase with the FLIP/PIC ratio and by increasing the ratio $\Delta t/\Delta x$. Such oscillations in space can be seen in the longitudinal stress profile in Figure 6. More advanced interpolation schemes, such as APIC (Jiang et al., 2016), could improve accuracy while preserving stability.

Finally, most of the presented simulation outputs have been found independent of the mesh resolution (critical crack length, distance for slab fracture, crack propagation speed, avalanche shape) provided the grid size Δx is small than the characteristic elastic length Λ . In addition, as expected and reported from 3D simulations, the arrest of crack propagation in the weak layer during slab fracture (Figure 7b) is mesh-dependent. This is related to the plastic strain-softening behavior of the slab. In the future, a regularized model could lead to some improvements in this direction (Mahajan et al., 2010; Sulsky & Peterson, 2011).

5. Conclusion and Outlook

In this article, we developed a rigorous mathematical framework based on the depth-averaged Material Point Method (DAMPM) to investigate large-scale crack propagation mechanisms involved in the release of shallow landslides. The model is applied to snow slab avalanches that release due to the failure of a weak layer buried below a cohesive snow slab. Motivated by recent findings revealing an early transition from anticrack (mode I) to supershear (mode II) crack propagation, we chose to simulate the weak layer with a pure shear failure model. We checked the validity of DAMPM by simulating simple test cases for which analytic solutions exist. The model was applied to slope-scale simulations to study the interplay between down/up slope propagation, cross slope propagation in the weak layer and slab fracture. We obtained avalanche release shapes qualitatively in good agreement with field observations. In the future, more complex topographies and the influence of the spatial variability of snowpack properties, for instance based on remote sensing data, should be considered to bring the proposed model at an operational state for automatic evaluation of avalanche release zones in alpine regions. This achievement could contribute to define avalanche size indices for avalanche forecasting and also serve as input of avalanche flow models used for risk assessment. Finally, it would be straightforward to modify the constitutive model and interface friction law assumed here to be able to simulate different processes, for instance the dynamics of avalanches or other types of gravitational mass movements, snow creep and its impact on structures, glacier flow and calving. In particular, the present approach would naturally account for active/passive lateral earth pressures through the plastic law without the need of empirical earth pressure coefficients.

Appendix A: Space Discretization of the DAMPM

In the same spirit of the FEM, we seek a weak form of the depth-averaged equations. To this end, we multiply Equations 11 and 12 by two test function w_x and w_y and then integrate over the domain Ω . Note that the rigorous formalism of which functional space the functions belong will not be outlined in this work. We use the same notation as in Abe and Konagai (2016) with $d\Omega$ being the infinitesimal element of integration.

$$\begin{aligned}\int_{\Omega} \rho h \frac{d\bar{v}_x}{dt} w_x d\Omega &= \int_{\Omega} \left[\frac{\partial h \bar{\sigma}_{xx}}{\partial x} + \frac{\partial h \bar{\sigma}_{xy}}{\partial y} \right] w_x d\Omega - \int_{\Omega} \tau_{xz} w_x d\Omega + \int_{\Omega} b_x \rho h w_x d\Omega \\ \int_{\Omega} \rho h \frac{d\bar{v}_y}{dt} w_y d\Omega &= \int_{\Omega} \left[\frac{\partial h \bar{\sigma}_{xy}}{\partial x} + \frac{\partial h \bar{\sigma}_{yy}}{\partial y} \right] w_y d\Omega - \int_{\Omega} \tau_{yz} w_y d\Omega + \int_{\Omega} b_y \rho h w_y d\Omega\end{aligned}$$

Using Green's theorem we have

$$\begin{aligned}\int_{\Omega} \rho h \frac{d\bar{v}_x}{dt} w_x d\Omega &= - \int_{\Omega} h \bar{\sigma}_{xx} \frac{\partial w_x}{\partial x} d\Omega - \int_{\Omega} h \bar{\sigma}_{xy} \frac{\partial w_x}{\partial y} d\Omega - \int_{\Omega} \tau_{xz} w_x d\Omega + \int_{\Omega} b_x \rho h w_x d\Omega \\ \int_{\Omega} \rho h \frac{d\bar{v}_y}{dt} w_y d\Omega &= - \int_{\Omega} h \bar{\sigma}_{xy} \frac{\partial w_y}{\partial x} d\Omega - \int_{\Omega} h \bar{\sigma}_{yy} \frac{\partial w_y}{\partial y} d\Omega - \int_{\Omega} \tau_{yz} w_y d\Omega + \int_{\Omega} b_y \rho h w_y d\Omega\end{aligned}$$

We define then $\tau_b^S = \frac{1}{h} \tau_b$ such that

$$\int_{\Omega} \rho h \frac{d\bar{v}_x}{dt} w_x d\Omega = - \int_{\Omega} h \bar{\sigma}_{xx} \frac{\partial w_x}{\partial x} d\Omega - \int_{\Omega} h \bar{\sigma}_{xy} \frac{\partial w_x}{\partial y} d\Omega - \int_{\Omega} h \tau_{xz}^S w_x d\Omega + \int_{\Omega} b_x \rho h w_x d\Omega \quad (A1)$$

$$\int_{\Omega} \rho h \frac{d\bar{v}_y}{dt} w_y d\Omega = - \int_{\Omega} h \bar{\sigma}_{xy} \frac{\partial w_y}{\partial x} d\Omega - \int_{\Omega} h \bar{\sigma}_{yy} \frac{\partial w_y}{\partial y} d\Omega - \int_{\Omega} h \tau_{yz}^S w_y d\Omega + \int_{\Omega} b_y \rho h w_y d\Omega \quad (A2)$$

We decompose our material in n_p columns. These columns will move with the material during the simulation. As in standard MPM, we assume that the mass is concentrated at each column. We have then

$$\forall \mathbf{x} \in \Omega, t \in \mathbb{R}_+, \quad \rho(\mathbf{x}, t) h(\mathbf{x}, t) = \sum_{p=1}^{n_p} m_p \delta(\mathbf{x} - \mathbf{x}_p) \quad (A3)$$

where δ is the Dirac distribution with dimension of inverse of a surface and \mathbf{x}_p is the position of the column p . Note that \mathbf{x}_p is a function of time. Here, because we assume that the material is incompressible, this simplifies to

$$\forall \mathbf{x} \in \Omega, t \in \mathbb{R}_+, \quad h(\mathbf{x}, t) = \sum_{p=1}^{N_p} V_p \delta(\mathbf{x} - \mathbf{x}_p), \quad (A4)$$

with V_p is the constant volume of the column.

Until the end of this subsection, we present the discretization only for Equation A1, however, the discretization for Equation A2 is analogous. Inserting Equation A4 into Equation A1, we have

$$\begin{aligned}\sum_p \rho V_p \bar{a}_{x,p} w_{x,p} &= - \sum_p V_p \bar{\sigma}_{xx,p} \frac{\partial w_{x,p}}{\partial x} - \sum_p V_p \bar{\sigma}_{xy,p} \frac{\partial w_{x,p}}{\partial y} \\ &\quad - \sum_p V_p \tau_{xz,p}^S w_{x,p} + \sum_p V_p b_{x,p} \rho w_{x,p}\end{aligned}$$

where again the subscript p of a quantity correspond to its evaluation in \mathbf{x}_p . We can apply this discretization at any time t^k , denoting for any function ϕ , $\phi^k = \phi(t^k)$, the previous equation gives

$$\begin{aligned}\sum_p \rho V_p \bar{a}_{x,p}^k w_{x,p} &= - \sum_p V_p \bar{\sigma}_{xx,p}^k \frac{\partial w_{x,p}}{\partial x} - \sum_p V_p \bar{\sigma}_{xy,p}^k \frac{\partial w_{x,p}}{\partial y} \\ &\quad - \sum_p A_p \tau_{xz,p}^k w_{x,p} + \sum_p \rho V_p b_{x,p}^k w_{x,p}\end{aligned} \quad (A5)$$

where $A_p = V_p/h$ is the area of the column p . We want to perform the computation on the grid node. To this end, we introduce interpolation functions $N_i(\mathbf{x})$ centered on node $i \in \{1, \dots, n_g\}$. We can then approximate

$$\bar{a}_{x,p}^k = \sum_{i=1}^{n_g} \bar{a}_{x,i}^k N_{ip}^k, \quad w_{x,p} = \sum_{i=1}^{n_g} w_{x,i} N_{ip}^k, \quad (\text{A6})$$

where $\bar{a}_{x,i}^k = \bar{a}_x(\mathbf{x}_i, t^k)$, $N_{ip}^k = N_i(\mathbf{x}_p(t^k))$ and $w_{x,i} = w_x(\mathbf{x}_i)$. The gradients can be interpolated as well with the equality

$$\nabla w_{x,p} = \sum_{i=1}^{n_g} w_{x,i} \nabla N_{ip}^k, \quad \nabla N_{ip}^k = \nabla N_i(\mathbf{x}_p(t^k))$$

Note that the function N must satisfy the following conditions (Gao et al., 2017):

- Partition of unity: $\sum_i N_{ip}^k = 1, \forall p \in \{1, \dots, n_p\}$
- Non-negativity: $N_{ip}^k \geq 0, \forall p \in \{1, \dots, n_p\}$ and $\forall i \in \{1, \dots, n_g\}$
- Differentiability: $N_i \in C^1, \forall i \in \{1, \dots, n_g\}$
- Interpolation: $\mathbf{x}_p = \sum_i N_{ip}^k \mathbf{x}_i$
- Local support: $N_{ip}^k > 0$ only if \mathbf{x}_i and \mathbf{x}_p are close enough

We can now express Equation A5 with quantities over the grid

$$\begin{aligned} \sum_{p=1}^{n_p} \sum_{i=1}^{n_g} \sum_{j=1}^{n_g} \rho V_p \bar{a}_{x,j}^k N_{jp}^k w_{x,i} N_{ip}^k &= - \sum_{p=1}^{n_p} \sum_{i=1}^{n_g} V_p \bar{\sigma}_{xx,p}^k w_{x,i} \frac{\partial N_{ip}^k}{\partial x} - \sum_{p=1}^{n_p} \sum_{i=1}^{n_g} V_p \bar{\sigma}_{xy,p}^k \frac{\partial N_{ip}^k}{\partial y} w_{x,i} \\ &\quad - \sum_{p=1}^{n_p} \sum_{i=1}^{n_g} A_p \tau_{xz,p}^k w_{x,i} N_{ip}^k + \sum_{p=1}^{n_p} \sum_{i=1}^{n_g} \rho V_p b_{x,p}^k w_{x,i} N_{ip}^k \end{aligned}$$

Defining the mass matrix at time k as

$$m_{ij}^k = \sum_{p=1}^{n_p} m_p N_{ip}^k N_{jp}^k$$

where $m_p^k = \rho V_p^k$ is the mass of the column p , the system becomes

$$\begin{aligned} \sum_{i=1}^{n_g} \sum_{j=1}^{n_g} m_{ij}^k \bar{a}_{x,j}^k w_{x,i} &= - \sum_{i=1}^{n_g} \left[\sum_{p=1}^{n_p} \left[V_p \bar{\sigma}_{xx,p}^k \frac{\partial N_{ip}^k}{\partial x} + V_p \bar{\sigma}_{xy,p}^k \frac{\partial N_{ip}^k}{\partial y} \right] \right] w_{x,i} \\ &\quad - \sum_{i=1}^{n_g} \left[\sum_{p=1}^{n_p} A_p \tau_{xz,p}^k N_{ip}^k \right] w_{x,i} + \sum_{i=1}^{n_g} \left[\sum_{p=1}^{n_p} \rho V_p b_{x,p}^k N_{ip}^k \right] w_{x,i}. \end{aligned}$$

As the interpolation functions satisfy $\sum_{i=1}^{n_g} N_{ip}^k = 1$, the mass matrix can be approximated by a symmetric positive diagonal matrix (the so-called lumped mass approach) (Jiang et al., 2016), such that

$$\sum_{j=1}^{n_g} m_{ij}^k \bar{a}_{x,j}^k \approx m_i^k \bar{a}_{x,i}^k$$

where

$$m_i^k = \sum_{j=1}^{n_g} m_{ij}^k$$

gives the mass at node i .

Defining the internal forces $f_{x,i}^{\text{int},k}$ and the external forces $f_{x,i}^{\text{ext},k}$ for every $i \in \{1, \dots, n_g\}$ as

$$f_{x,i}^{\text{ext},k} = \sum_{p=1}^{n_p} \rho V_p b_{x,p}^k N_{ip}^k \quad (\text{A7})$$

$$f_{x,i}^{\text{int},k} = - \sum_{p=1}^{n_p} \left[V_p \bar{\sigma}_{xx,p}^k \frac{\partial N_{ip}^k}{\partial x} + V_p \bar{\sigma}_{xy,p}^k \frac{\partial N_{ip}^k}{\partial y} + \tau_{xz,p}^k N_{ip}^k \right] \quad (\text{A8})$$

the discretized equation becomes

$$\sum_{i=1}^{n_g} m_i^k \bar{a}_{x,i}^k w_{x,i} = \sum_{i=1}^{n_g} (f_{x,i}^{\text{ext},k} + f_{x,i}^{\text{int},k}) w_{x,i}.$$

This relation being true for every sequences $(w_{x,i})_{i \in \{1, \dots, n_g\}}$, we have the equality for each term.

$$m_i^k \bar{a}_{x,i}^k = (f_{x,i}^{\text{ext},k} + f_{x,i}^{\text{int},k}) \quad \forall i \in \{1, \dots, n_g\}. \quad (\text{A9})$$

Appendix B: DAMPM Algorithm

This Appendix consists of a summary of Section 2.2.2.

Algorithm 1. Depth-Averaged Material Point Method (DAMPM)

while $t < T$ **do**

1. Create/expand/reduce the Eulerian grid around the particle domain
2. P2G: interpolate particle velocity and mass to the grid with Equation 24
3. Compute grid forces f_i^{int} and f_i^{ext} with Equations 22 and 23 depending on $\bar{\sigma}_p$, $\tau_{xz,p}$, $\tau_{yz,p}$, and \mathbf{b}_p
4. Compute grid acceleration \mathbf{a}_i with Equation 26 and grid velocity \mathbf{v}_i^L with Equation 27
5. G2P: update the particle velocity \mathbf{v}_p and position \mathbf{x}_p with Equations 28 and 29
6. Update the grid velocity \mathbf{v}_i from particle velocity with Equation 30
7. Compute the strain tensor $\Delta \epsilon_p^{\text{trial}}$ with Equation 31
8. Update the height h_p with Equation 32
9. Compute the stress $\bar{\sigma}_p^{\text{trial}}$ with Equation 33
10. Compute the yield criterion $f(p(\bar{\sigma}_p^{\text{trial}}), q(\bar{\sigma}_p^{\text{trial}}))$ with Equation 18

if $f(p(\bar{\sigma}_p^{\text{trial}}), q(\bar{\sigma}_p^{\text{trial}})) \leq 0$ **then**

update the stress $\bar{\sigma}_p$ with Equation 35

else

set the stress $\bar{\sigma}_p$ to 0

end if

11. Adapt Δt according to with Equations 36 and 37 and update time $t = t + \Delta t$

end while

Appendix C: Depth Integration on Complex Topography

In the previous integration, we supposed that the terrain was flat. In order to simulate the material on a complex terrain we have to change the previous equation by adding in the depth-averaged momentum conservation some terms depending on the surface gradients. However, for an arbitrary topography, it is more relevant to pass from cartesian coordinates to curvilinear coordinates, adapted to the topography. This will allow us to integrate the equations according to the surface normal. For the change of coordinates and the integration which follows, we shall use the same notation as the one introduced in Boutounet et al. (2008) and Bouchut and

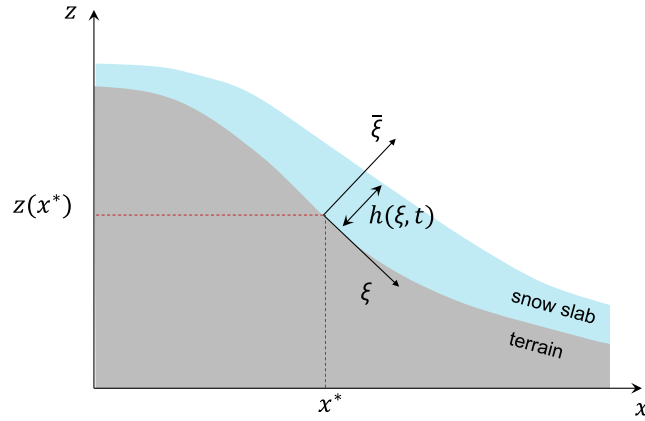


Figure C1. Illustration of the new set of variable (ξ, ξ_n) following the slope topography.

Westdickenberg (2004). Thus the notation ϕ_n denote the vertical component of a vector $\vec{\phi} = \begin{pmatrix} \phi \\ \phi_n \end{pmatrix}$, where ϕ is the tangential vector (Figure C1).

We denote $\mathbf{x} \in \mathbb{R}^N$ the horizontal cartesian coordinates ($N = 1$ or $N = 2$ according of the modeling) and $\xi \in \mathbb{R}^N$ the tangential curvilinear coordinates which can be seen as of function of the variable \mathbf{x} . The $N \times N$ matrix $\partial_{\xi}\mathbf{x}$ represent the jacobian matrix of the function \mathbf{x} .

If the bottom surface S is the graph of a function $z : \mathbb{R}^N \rightarrow \mathbb{R}$, that is, $S = \{(\mathbf{x}, z(\mathbf{x})), \mathbf{x} \in \mathbb{R}^N\}$, we can easily define the normal \mathbf{n} to S as

$$\mathbf{n} = \begin{pmatrix} -s \\ c \end{pmatrix}, \quad s = (1 + \|\nabla_x z\|^2)^{-\frac{1}{2}} \nabla_x z, \quad c = (1 + \|\nabla_x z\|^2)^{-\frac{1}{2}}$$

In the previous equation, ∇_x represents the gradient with respect to the variable \mathbf{x} . Note that since \mathbf{n} is unitary, we have the following relation $\|\mathbf{n}\|^2 = \|s\|^2 + c^2 = 1$. This leads to the following equation

$$\partial_x c = -\frac{1}{c} s' \partial_x s, \quad \partial_x s = c(1 - s' s) \partial_{xx} z, \quad \partial_{xx}^2 z = \frac{c^2 \mathbf{I} + s s^t}{c^3} \partial_x s \quad (\text{C1})$$

We then define a new system of coordinate $\vec{\xi} = (\xi, \xi_n)$ where ξ_n is the coordinate along the normal to the bed S . If Ω_t is the fluid domain at time t , we have

$$\vec{X}(\vec{\xi}) \in \Omega_t \Leftrightarrow \vec{X}(\vec{\xi}) = \begin{pmatrix} \mathbf{x}(\xi) \\ z(\mathbf{x}(\xi)) \end{pmatrix} + \xi_n \mathbf{n}(\mathbf{x}(\xi)), \quad 0 \leq \xi_n \leq h(\xi, t)$$

We can now define new velocity components \vec{V} with respect of the new coordinates, if we denote by \vec{U} the velocity field in the Cartesian base, we have

$$\vec{U} = \left(\partial_{\xi} \vec{X} \right) \vec{V} \quad (\text{C2})$$

with

$$\partial_{\xi} \vec{X} = \begin{pmatrix} \partial_{\xi} \mathbf{x} & -s \\ \frac{1}{c} s' (\partial_{\xi} \mathbf{x}) & c \end{pmatrix} \in \mathcal{M}_{n+1}(\mathbb{R}) \quad (\text{C3})$$

and

$$\partial_{\xi} X = (I - \xi_n \partial_x s) \partial_{\xi} x \in \mathcal{M}_n(\mathbb{R}) \quad (C4)$$

We denote $A = \left(\partial_{\xi} \vec{X} \right)^{-1} \in \mathcal{M}_{n+1}(\mathbb{R})$. Inserting Equations C3 and C1, we have

$$A = \begin{pmatrix} (\partial_{\xi} X)^{-1} & 0 \\ 0 & 1 \end{pmatrix} \begin{pmatrix} I - ss' & cs \\ -s'(\partial_{\xi} X) & c \end{pmatrix} \quad (C5)$$

We can then compute the matrix $\tilde{M} = AA^t \in \mathcal{M}_{n+1}(\mathbb{R})$, which can be rewritten as

$$\tilde{M} = \begin{pmatrix} M & 0 \\ 0 & 1 \end{pmatrix}, \quad M = (\partial_{\xi} X)^{-1} (I - ss') (\partial_{\xi} X)^{-t} \quad (C6)$$

and we now compute the jacobian J of the coordinates transformation:

$$J = \det \left(\partial_{\xi} \vec{X} \right) = \frac{1}{c} \det(\partial_{\xi} X) = \det(M)^{-\frac{1}{2}}. \quad (C7)$$

The change of variable will induce a change of the differentiable operator used in the governing equations. This result is the Lemma 1 of Boutounet et al. (2008) and the proof can be found in Bouchut and Westdickenberg (2004). For any field \vec{Z} , the differential operator transform to

$$J \nabla_{\vec{X}} \cdot \vec{Z} = \nabla_{\vec{\xi}} \cdot (JA \vec{Z}), \quad \vec{U} \cdot \nabla_{\vec{X}} = \vec{V} \cdot \nabla_{\vec{\xi}}, \quad \nabla_{\vec{X}} = A^t \nabla_{\vec{\xi}} \quad (C8)$$

and for any symmetric tensor σ ,

$$JA^{-t} \nabla_{\vec{X}} \cdot \sigma = \nabla_{\vec{\xi}} (JPAA^t) + \frac{J}{2} \mathcal{P} : \nabla_{\vec{\xi}} \tilde{M}, \quad \text{with } \mathcal{P} = A^{-t} \sigma A^{-1} \quad (C9)$$

We notice that the tensor \mathcal{P} is the stress tensor oriented in the curvilinear coordinates.

C1. Boundary Conditions

We have the same kinematic condition as with the cartesian coordinates, that is,

$$\partial_t h + V_h \cdot \nabla_{\vec{\xi}} h = \bar{V}_h \quad (C10)$$

with the following notation for a field ϕ , $\phi_h(\xi) = \phi(\xi, h(\xi, t))$.

The stress free condition yields that for $\vec{\xi} = h(\xi, t)$, no forces are apply on the slab, this means

$$\sigma_h = 0 \quad (C11)$$

C2. Governing Equation in New Coordinates

In the incompressible case, the mass conservation is reduced to $\nabla_{\vec{X}} \cdot \vec{U} = 0$. Multiplying this equation by J and use Equation C8, we get

$$\nabla_{\vec{\xi}} \cdot (J \vec{V}) = \nabla_{\vec{\xi}} \cdot (JV) + \partial_{\vec{\xi}} J \bar{V} = 0 \quad (C12)$$

The equation translating the momentum conservation is, in cartesian coordinates

$$\partial_t \vec{U} + \vec{U} \cdot \nabla_{\vec{X}} \vec{U} = -\vec{g} + \frac{1}{\rho} \nabla_{\vec{X}} \cdot \sigma. \quad (C13)$$

If we multiply Equation C13 by matrix A and use the curvilinear operators, one finds

$$\partial_t \vec{V} + \vec{V} \cdot \nabla_{\vec{\xi}} \vec{V} = -A\vec{g} + \vec{\Gamma}(\vec{V}) + \frac{1}{\rho J} \tilde{M} \left(\nabla_{\vec{\xi}} \cdot (J \mathcal{P} \tilde{M}) + \frac{J}{2} \mathcal{P} : \nabla_{\vec{\xi}} \tilde{M} \right) \quad (C14)$$

The term $\vec{\Gamma}(\vec{V})$ is a correction induced by the change of coordinate in the convective term, we have

$$\vec{\Gamma}(\vec{V}) = A\vec{V} \cdot \nabla_{\vec{\xi}} (A^{-1} \vec{V}) - \vec{V} \cdot \nabla_{\vec{\xi}} \vec{V} \quad (C15)$$

This term will be neglected in the next section. In order to simplify the notation and highlight the different component of the tensor stress \mathcal{P} , we decompose

$$\mathcal{P} = \begin{pmatrix} P & Z \\ Z^t & \sigma_{\vec{\xi}} \end{pmatrix} \quad (C16)$$

P_{ij} corresponds to $\xi_i \xi_j$ direction of the stress tensor and Z corresponds to the shear in the $\xi_i \vec{\xi}$ direction.

If we projected Equation C15 in the (ξ_1, \dots, ξ_n) direction we have

$$\partial_t V + \vec{V} \cdot \nabla_{\vec{\xi}} V = -gc(\partial_{\vec{\xi}} X)^{-1} s + \Gamma(\vec{V}) + \frac{1}{\rho J} M \left(\nabla_{\vec{\xi}} \cdot (J P M) + \partial_{\vec{\xi}} J Z + \frac{J}{2} P : \nabla_{\vec{\xi}} M \right) \quad (C17)$$

The latter equation is almost the same equation as the momentum conservation equation in curvilinear coordinates found in Boutounet et al. (2008). However, in order to model an elasto-plastic behavior of the slab, no further hypothesis will be assumed on the stress tensor \mathcal{P} , which will be namely the one use in the elastic constitutive law.

C3. Shallow Water and Small Velocity Hypothesis

We can express the shallow water hypothesis with the new set of coordinates (Bouchut & Westdickenberg, 2004), which are namely

- The height of the material is small comparing to ε , $h = \mathcal{O}(\varepsilon)$
- The curvature is small comparing to ε , $(\partial_{xx}^2 z) = \mathcal{O}(\varepsilon)$
- The velocity field does not depend on the depth of the material, $\vec{V}(t, \vec{\xi}) = V(t, \xi) + \mathcal{O}(\varepsilon)$

With this hypothesis, we have

$$\partial_{\vec{\xi}} X = \partial_{\xi} x + \mathcal{O}(\varepsilon^2)$$

which implies that

$$J = \bar{J} + \mathcal{O}(\varepsilon^2), \quad M = \bar{M} + \mathcal{O}(\varepsilon^2) \quad (C18)$$

with

$$\bar{M} = (\partial_{\xi} x)^{-1} (I - ss^t) (\partial_{\xi} x)^{-t}, \quad \bar{J} = \det(\bar{M})^{-\frac{1}{2}}. \quad (C19)$$

Equation C17 can thus be rewritten as

$$\partial_t V + \vec{V} \cdot \nabla_{\vec{\xi}} V = -gc(\partial_{\xi} x)^{-1} s + \Gamma(\vec{V}) + \frac{1}{\rho J} \bar{M} \left(\nabla_{\vec{\xi}} \cdot (J P \bar{M}) + \partial_{\vec{\xi}} \bar{J} Z + \frac{\bar{J}}{2} P : \nabla_{\vec{\xi}} \bar{M} \right). \quad (C20)$$

C4. Small Velocity

In this work, we want to simulate initiation of snow slab avalanches. In this process, we have a fast propagation of stress within the slab but the particles in slab have a very small velocity. The term $\Gamma(\vec{V})$ varies as the square of the velocity norm and thus will be neglected in this framework.

C5. Depth-Averaged Equation for the Quasi-1D Case

The integration of Equation C15 is strongly inspired from Bouchut and Westdickenberg (2004) and Boutounet et al. (2008). In this section, we will suppose the terrain varies only in one dimension (we suppose x). The function z representing the height of the bed does not depend of the variable y , that is,

$$\forall x, y \in \mathbb{R}, \frac{\partial z}{\partial y}(x, y) = 0.$$

We denote then $\theta = \arctan\left(\frac{\partial z}{\partial x}\right)$ such that $\partial_\xi \mathbf{x}$ can be rewritten as

$$\partial_\xi \mathbf{x} = \begin{pmatrix} \cos \theta & 0 \\ 0 & 1 \end{pmatrix}, \quad \text{and} \quad \mathbf{s} = \begin{pmatrix} \sin \theta \\ 0 \end{pmatrix} \quad (\text{C21})$$

Inserting this in Equation C19, we have

$$\overline{M} = \mathbf{I} \quad \overline{J} = \det(\overline{M}) = 1 \quad (\text{C22})$$

Equation C20 becomes then

$$\partial_t V + \vec{V} \cdot \nabla_\xi V = -gc(\partial_\xi \mathbf{x})^{-1} \mathbf{s} + \Gamma(\vec{V}) + \frac{1}{\rho} (\nabla_\xi \cdot \mathbf{P} + \partial_\xi Z).$$

Finally, by neglecting the term $\Gamma(\vec{V})$, the system becomes

$$\partial_t V + \vec{V} \cdot \nabla_\xi V = -gc(\partial_\xi \mathbf{x})^{-1} \mathbf{s} + \frac{1}{\rho} (\nabla_\xi \cdot \mathbf{P} + \partial_\xi Z). \quad (\text{C23})$$

Equation C23 has the exact same form as Equations 11 and 12. Therefore, the integrated equation will have the exact same form, namely

$$\partial_t h + \nabla_\xi (h\bar{v}) = 0 \quad (\text{C24})$$

$$\partial_t h\bar{v} + \nabla_\xi (h\bar{v} \times \bar{v}) = -hgc(\partial_\xi \mathbf{x})^{-1} \mathbf{s} + \frac{1}{\rho} \nabla_\xi \cdot (h\bar{\sigma}) + \frac{1}{\rho} Z_0. \quad (\text{C25})$$

with

$$\bar{v} = \int_0^{h(\xi,t)} V d\xi, \quad \bar{\sigma} = \int_0^{h(\xi,t)} P d\xi, \quad Z_0 = Z(\xi = 0).$$

Note that we have an explicit form for the product $c(\partial_\xi \mathbf{x})^{-1} \mathbf{s}$

$$c(\partial_\xi \mathbf{x})^{-1} \mathbf{s} = \mathbf{s} = \begin{pmatrix} \sin \theta \\ 0 \end{pmatrix}$$

Appendix D: Symbols and Notations

See Table D1.

Table D1

Table of Main Notation Used Within This Framework

	Symbol	Meaning	Unit
Slab	σ	Cauchy stress	kPa
	u	Displacement	m
	v	Velocity	ms ⁻¹
	ϵ	Strain	—
	x	Position	m
	b	Volumetric forces	Nm ⁻³
	D	Elastic 4th order stiffness tensor	kPa
	E	Young's modulus	MPa
	ν	Poisson's ratio	—
	(p_0, β, M)	Plastic parameters (Cohesive Cam Clay)	(kPa, —, —)
	θ	Slope angle	°
	h	Height	m
	ρ	Density	kgm ⁻³
	m	Mass	kg
	p	Hydrostatic pressure	kPa
	q	Von Mises equivalent stress	kPa
	ϕ	Basal frictional angle	°
Weak layer	D_{WL}	Thickness	m
	C_{WL}	Cohesion	kPa
	k_{WL}	Stiffness	Nm ⁻¹
	Λ	Characteristic length	m
	τ_{peak}	Shear strength	kPa
Numerical	u_c	Critical displacement	m
	Δx	Mesh size	m
	Δt	Time step	s
	C_{cfl}	CFL constraint	—
	$C_{elastic}$	Elastic constraint	—
General	C_{flip}	FLIP/PIC constraint	—
	$\frac{\partial \bullet}{\partial \xi}$	Partial derivative w.r.t. ξ	
	$\nabla(\bullet)$	Gradient	
	$\nabla \cdot (\bullet)$	Divergence	
	$\bar{\bullet}$	Depth-averaged	
	$\frac{D\bullet}{Dt}$	Material derivative	
	\bullet_p	Related to the material element p	
	\bullet_i	Related to the grid node i	
	\bullet_j	Related to the grid node j	
	\bullet_p	Related to plastic deformation	
	\bullet_E	Related to elastic deformation	
	N_i	Shape function centered at x_i	

Data Availability Statement

The codes developed in this study (C++) as well as some post-processing tools (python and houdini files) are available on Zenodo at the following link: <https://doi.org/10.5281/zenodo.7561750>.

Acknowledgments

This work was supported by the Swiss National Science Foundation (Grant PCEFP2_181227). Open access funding provided by Eidgenössische Technische Hochschule Zurich.

References

- Abe, K., & Konagai, K. (2016). Numerical simulation for runout process of debris flow using depth-averaged material point method. *Soils and Foundations*, 56(5), 869–888. <https://doi.org/10.1016/j.sandf.2016.08.011>
- Ancey, C. (2006). *Dynamique des avalanches*. PPUR Presses Polytechniques.
- Bergfeld, B., van Herwijnen, A., Bobillier, G., Larose, E., Moreau, L., Trottet, B., et al. (2022). Crack propagation speeds in weak snowpack layers. *Journal of Glaciology*, 68(269), 557–570. <https://doi.org/10.1017/jog.2021.118>
- Bizzarri, A., & Das, S. (2012). Mechanics of 3-D shear cracks between Rayleigh and shear wave rupture speeds. *Earth and Planetary Science Letters*, 357–358, 397–404. <https://doi.org/10.1016/j.epsl.2012.09.053>
- Blatny, L., Berclaz, P., Guillard, F., Einav, I., & Gaume, J. (2022). Microstructural origin of propagating compaction patterns in porous media. *Physical Review Letters*, 128(22), 228002. <https://doi.org/10.1103/PhysRevLett.128.228002>
- Blatny, L., Löwe, H., Wang, S., & Gaume, J. (2021). Computational micromechanics of porous brittle solids. *Computers and Geotechnics*, 140, 104284. <https://doi.org/10.1016/j.compgeo.2021.104284>
- Bobillier, G., Bergfeld, B., Dual, J., Gaume, J., van Herwijnen, A., & Schweizer, J. (2021). Micro-mechanical insights into the dynamics of crack propagation in snow fracture experiments. *Scientific Reports*, 11(1), 2045–2322. <https://doi.org/10.1038/s41598-021-90910-3>
- Bouchut, F., & Westdickenberg, M. (2004). Gravity driven shallow water model for arbitrary topography. *Communications in Mathematical Sciences*, 3, 359–389. <https://doi.org/10.4310/cms.2004.v2.n3.a2>
- Boutounet, M., Chupin, L., Noble, P., & Vila, J.-P. (2008). Shallow water viscous flows for arbitrary topography. *Communications in Mathematical Sciences*. <https://doi.org/10.1016/j.ijssolstr.2017.12.033>
- Broberg, K. B. (1989a). How fast can a crack go? *Materials Science*, 32(1), 80–86. <https://doi.org/10.1007/BF02538928>
- Broberg, K. B. (1989b). The near-tip field at high crack velocities. *International Journal of Fracture*, 39(1–3), 1–13. <https://doi.org/10.1007/BF00047435>
- Cicoira, A., Blatny, L., Li, X., Trottet, B., & Gaume, J. (2022). Towards a predictive multi-phase model for alpine mass movements and process cascades. *Engineering Geology*, 310, 106866. <https://doi.org/10.1016/j.enggeo.2022.106866>
- Daviet, G., & Bertails-Descoubes, F. (2016). A semi-implicit material point method for the continuum simulation of granular materials. *ACM Transactions on Graphics*, 35(4), 1–13. <https://doi.org/10.1145/2897824.2925877>
- de Souza Neto, E. A., Peric, D., & Owen, D. R. J. (2008). *Computational methods for plasticity*. Springer.
- Dunatunga, S., & Kamrin, K. (2015). Continuum modelling and simulation of granular flows through their many phases. *Journal of Fluid Mechanics*, 779, 483–513. <https://doi.org/10.1017/jfm.2015.383>
- Faillietaz, J., Louchet, F., & Grasso, J.-R. (2006). Cellular automaton modelling of slab avalanche triggering mechanisms: From the universal statistical behavior to particular cases. In *International snow science workshop* (pp. 174–180).
- Fletcher, R. C., & Pollard, D. D. (1981). Anticrack model for pressure solution surfaces. *Geology*, 9(9), 419–424. [https://doi.org/10.1130/0091-7613\(1981\)9<419:amfss>2.0.co;2](https://doi.org/10.1130/0091-7613(1981)9<419:amfss>2.0.co;2)
- Fyffe, B., & Zaiser, M. (2004). The effects of snow variability on slab avalanche release. *Cold Regions Science and Technology*, 40(3), 229–242. <https://doi.org/10.1016/j.coldregions.2004.08.004>
- Fyffe, B., & Zaiser, M. (2007). Interplay of basal shear fracture and slab rupture in slab avalanche release. *Cold Regions Science and Technology*, 49(1), 26–38. (Selected Papers from the General Assembly of the European Geosciences Union (EGU)). <https://doi.org/10.1016/j.coldregions.2006.09.011>
- Gao, M., Tampubolon, A. P., Jiang, C., & Sifakis, E. (2017). An adaptive generalized interpolation material point method for simulating elastoplastic materials. *ACM Transactions on Graphics*, 36(6), 1–12. <https://doi.org/10.1145/3130800.3130879>
- Gaume, J., Chambon, G., Eckert, N., & Naaim, M. (2013a). Influence of weak-layer heterogeneity on snow slab avalanche release: Application to the evaluation of avalanche release depths. *Journal of Glaciology*, 59(215), 423–437. <https://doi.org/10.3189/2013JG12J161>
- Gaume, J., Chambon, G., Eckert, N., Naaim, M., & Schweizer, J. (2015). Influence of weak layer heterogeneity and slab properties on slab tensile failure propensity and avalanche release area. *The Cryosphere*, 9(2), 795–804. <https://doi.org/10.5194/tc-9-795-2015>
- Gaume, J., Eckert, N., Chambon, G., Naaim, M., & Bel, L. (2013). Mapping extreme snowfalls in the French alps using max-stable processes. *Water Resources Research*, 49(2), 1079–1098. <https://doi.org/10.1002/wrcr.20083>
- Gaume, J., Gast, T., Terran, J., Van Herwinjen, A., & Jiang, C. (2018). Dynamic anticrack propagation in snow. *Nature Communications*, 9(3047), 3047. <https://doi.org/10.1038/s41467-018-05181-w>
- Gaume, J., & Reuter, B. (2017). Assessing snow instability in skier-triggered snow slab avalanches by combining failure initiation and crack propagation. *Cold Regions Science and Technology*, 144, 6–15. (International Snow Science Workshop 2016 Breckenridge). <https://doi.org/10.1016/j.coldregions.2017.05.011>
- Gaume, J., van Herwijnen, A., Chambon, G., Birkeland, K. W., & Schweizer, J. (2015). Modeling of crack propagation in weak snowpack layers using the discrete element method. *The Cryosphere*, 9(5), 1915–1932. <https://doi.org/10.5194/tc-9-1915-2015>
- Gaume, J., van Herwijnen, A., Gast, T., Teran, J., & Jiang, C. (2019). Investigating the release and flow of snow avalanches at the slope-scale using a unified model based on the material point method. *Cold Regions Science and Technology*, 168, 102847. <https://doi.org/10.1016/j.coldregions.2019.102847>
- Gauthier, D., & Jamieson, B. (2008). Evaluation of a prototype field test for fracture and failure propagation propensity in weak snowpack layers. *Cold Regions Science and Technology*, 51(2), 87–97. <https://doi.org/10.1016/j.coldregions.2007.04.005>
- Heierli, J., Gumbsch, P., & Zaiser, M. (2008). Anticrack nucleation as triggering mechanism for snow slab avalanches. *Science*, 321(5886), 240–243. <https://doi.org/10.1126/science.1153948>
- Jamieson, J., & Johnston, C. (2001). Evaluation of the shear frame test for weak snowpack layers. *Annals of Glaciology*, 32, 59–69. <https://doi.org/10.3189/172756401781819472>
- Jiang, C., Schroeder, C., Teran, J., Stomakhin, A., & Selle, A. (2016). The material point method for simulating continuum materials. In *ACM siggraph 2016 courses*. Association for Computing Machinery.

- Johnson, B. C., Jamieson, J. B., & Stewart, R. R. (2004). Seismic measurement of fracture speed in a weak snowpack layer. *Cold Regions Science and Technology*, 40(1), 41–45. <https://doi.org/10.1016/j.coldregions.2004.05.003>
- Li, X., Sovilla, B., Jiang, C., & Gaume, J. (2021). Three-dimensional and real-scale modeling of flow regimes in dense snow avalanches. *Landslides*, 18(10), 3393–3406. <https://doi.org/10.1007/s10346-021-01692-8>
- Mahajan, P., Kalakuntla, R., & Chandel, C. (2010). Numerical simulation of failure in a layered thin snowpack under skier load. *Annals of Glaciology*, 51(54), 169–175. <https://doi.org/10.3189/172756410791386436>
- McClung, D. (1979). Shear fracture precipitated by strain softening as a mechanism of dry slab avalanche release. *Journal of Geophysical Research*, 84(B7), 3519–3526. <https://doi.org/10.1029/jb084ib07p03519>
- McClung, D., & Schaerer, P. A. (2006). *The avalanche handbook*. The Mountaineers Books.
- McClung, D. M. (2003). Size scaling for dry snow slab release. *Journal of Geophysical Research*, 108(B10), 2465. <https://doi.org/10.1029/2002JB002298>
- McClung, D. M. (2009). Dimensions of dry snow slab avalanches from field measurements. *Journal of Geophysical Research*, 114(F1), F01006. <https://doi.org/10.1029/2007JF000941>
- Mellor, M. (1975). *A review of basic snow mechanics* (Vol. 114, pp. 251–291). IAHS Publication.
- Meschke, G., Liu, C., & Mang, H. A. (1996). Large strain finite-element analysis of snow. *Journal of Engineering Mechanics*, 122(7), 591–602. [https://doi.org/10.1061/\(ASCE\)0733-9399\(1996\)122:7\(591\)](https://doi.org/10.1061/(ASCE)0733-9399(1996)122:7(591))
- Palmer, A., & Rice, J. (1973). The growth of slip surfaces in the progressive failure of over-consolidated clay. *Proceedings of the Royal Society of London, Series A: Mathematical and Physical Sciences*, 332, 527–548.
- Puzrin, A. M., Faug, T., & Einav, I. (2019). The mechanism of delayed release in earthquake-induced avalanches. *Proceedings of the Royal Society A*, 475(2227), 20190092. <https://doi.org/10.1098/rspa.2019.0092>
- Reiweger, I. (2011). Failure of a layer of buried surface hoar (Unpublished doctoral dissertation). ETH Zürich.
- Reiweger, I., Gaume, J., & Schweizer, J. (2015). A new mixed-mode failure criterion for weak snowpack layers. *Geophysical Research Letters*, 42(5), 1427–1432. <https://doi.org/10.1002/2014GL062780>
- Reuter, B., & Schweizer, J. (2018). Describing snow instability by failure initiation, crack propagation, and slab tensile support. *Geophysical Research Letters*, 45(14), 7019–7027. <https://doi.org/10.1029/2018GL078069>
- Roscoe, K., & Burland, J. (1968). On the generalized stress-strain behavior of wet clays. In J. Heyman, & F. Leckie (Eds.), *Engineering plasticity*. Cambridge University Press.
- Savage, S. B., & Hutter, K. (1915). The dynamics of avalanches of granular materials from initiation to runout. Part I: Analysis. *Acta Mechanica*, 86(1–4), 201–223. (Particle Simulation Methods). <https://doi.org/10.1007/BF01175958>
- Schreck, C., & Wojtan, C. (2020). A practical method for animating anisotropic elastoplastic materials. *Computer Graphics Forum*, 39(2), 89–99. <https://doi.org/10.1111/cgf.13914>
- Schweizer, J., Bruce Jamieson, J., & Schneebeli, M. (2003). Snow avalanche formation. *Reviews of Geophysics*, 41(4), 1016. <https://doi.org/10.1029/2002RG000123>
- Schweizer, J., Reuter, B., van Herwijnen, A., & Gaume, J. (2016). Avalanche release 101. In *International snow science workshop* (pp. 1–11).
- Sigrist, C. (2006). Measurements of fracture mechanical properties of snow and application to dry snow slab avalanche release (Unpublished doctoral dissertation). ETH Zürich.
- Soga, K., Alonso, E., Yerro, A., Kumar, K., & Bandara, S. (2016). Trends in large-deformation analysis of landslide mass movements with particular emphasis on the material point method. *Géotechnique*, 66(3), 248–273. <https://doi.org/10.1680/jgeot.15.LM.005>
- Stomakhin, A., Schroeder, C., Chai, L., Teran, J., & Selle, A. (2013). A material point method for snow simulation. *ACM Transactions on Graphics*, 32(4), 1–10. <https://doi.org/10.1145/2461912.2461948>
- Sulsky, D., Chen, Z., & Schreyer, H. (1994). A particle method for history-dependent materials. *Computer Methods in Applied Mechanics and Engineering*, 118(1), 179–196. [https://doi.org/10.1016/0045-7825\(94\)90112-0](https://doi.org/10.1016/0045-7825(94)90112-0)
- Sulsky, D., & Peterson, K. (2011). Toward a new elastic–decohesive model of arctic sea ice. *Physica D: Nonlinear Phenomena*, 240(20), 1674–1683. (Special Issue: Fluid Dynamics: From Theory to Experiment). <https://doi.org/10.1016/j.physd.2011.07.005>
- Sulsky, D., Zhou, S.-J., & Schreyer, H. (1995). Application of a particle-in-cell method to solid mechanics. *Computer Physics Communications*, 87(1), 236–252. (Particle Simulation Methods). [https://doi.org/10.1016/0010-4655\(94\)00170-7](https://doi.org/10.1016/0010-4655(94)00170-7)
- Trottet, B., Simenhois, R., Bobillier, G., Bergfeld, B., van Herwijnen, A., Jiang, C., & Gaume, J. (2022). Transition from sub-rayleigh anticrack to supershear crack propagation in snow avalanches. *Nature Physics*, 18(9), 1094–1098. <https://doi.org/10.1038/s41567-022-01662-4>
- van Herwijnen, A., Bair, E. H., Birkeland, K. W., Reuter, B., Simenhois, R., Jamieson, B., & Schweizer, J. (2016). Measuring the mechanical properties of snow relevant for dry-snow slab avalanche release using particle tracking velocimetry. In *International snow science workshop* (pp. 397–404).
- van Herwijnen, A., Gaume, J., Bair, E. H., Reuter, B., Birkeland, K. W., & Schweizer, J. (2016). Estimating the effective elastic modulus and specific fracture energy of snowpack layers from field experiments. *Journal of Glaciology*, 62(236), 997–1007. <https://doi.org/10.1017/jog.2016.90>
- Van Herwijnen, A., & Heierli, J. (2009). Measurement of crack-face friction in collapsed weak snow layers. *Geophysical Research Letters*, 36(23), L23502. <https://doi.org/10.1029/2009gl040389>
- van Herwijnen, A., & Jamieson, B. (2007). Snowpack properties associated with fracture initiation and propagation resulting in skier-triggered dry snow slab avalanches. *Cold Regions Science and Technology*, 50(1), 13–22. <https://doi.org/10.1016/j.coldregions.2007.02.004>
- Veitinger, J., Purves, R. S., & Sovilla, B. (2016). Potential slab avalanche release area identification from estimated winter terrain: A multi-scale, fuzzy logic approach. *Natural Hazards and Earth System Sciences*, 16(10), 2211–2225. <https://doi.org/10.5194/nhess-16-2211-2016>
- Vicari, H., Tran, Q. A., Nordan, S., & Thakur, V. (2022). Mpm modelling of debris flow entrainment and interaction with an upstream flexible barrier. *Landslides*, 19(9), 1–15. <https://doi.org/10.1007/s10346-022-01886-8>
- Weng, H., & Ampuero, J.-P. (2020). Continuum of earthquake rupture speeds enabled by oblique slip. *Nature Geoscience*, 13(12), 817–821. <https://doi.org/10.1038/s41561-020-00654-4>
- Wolper, J., Gao, M., Lüthi, M. P., Heller, V., Vieli, A., Jiang, C., & Gaume, J. (2021). A glacier–ocean interaction model for tsunami genesis due to iceberg calving. *Communications Earth & Environment*, 2(1), 1–10. <https://doi.org/10.1038/s43247-021-00179-7>
- York, A. R., II, Sulsky, D., & Schreyer, H. L. (2000). Fluid–membrane interaction based on the material point method. *International Journal for Numerical Methods in Engineering*, 48(6), 901–924. [https://doi.org/10.1002/\(SICI\)1097-0207\(20000630\)48:6<901::AID-NME910>3.0.CO;2-T](https://doi.org/10.1002/(SICI)1097-0207(20000630)48:6<901::AID-NME910>3.0.CO;2-T)
- Zhang, W., & Puzrin, A. M. (2022). How small slip surfaces evolve into large submarine landslides—Insight from 3D numerical modeling. *Journal of Geophysical Research: Earth Surface*, 127(7), e2022JF006640. <https://doi.org/10.1029/2022JF006640>